

1 Quantifying the Impact of SST Feedback Frequency on the 2 Madden-Julian Oscillation Simulations

3 Yung-Yao Lan¹, Huang-Hsiung Hsu¹, and Wan-Ling Tseng²

4 ¹Research Center for Environmental Changes, Academia Sinica, Taipei 11529, Taiwan

5 ²Ocean Center, National Taiwan University, Taipei 10617, Taiwan

6 Correspondence to: Huang-Hsiung Hsu (hhhsu@gate.sinica.edu.tw)

7

8 Abstract

9 This study uses the CAM5 coupled to a 1-d ocean model to investigate the effects
10 of intraseasonal SST feedback frequency on the Madden-Julian Oscillation (MJO)
11 simulation with intervals at 30 minutes, 1, 3, 6, 12, 18, 24, and 30 days. The large-scale
12 nature of the MJO in simulations remains intact with decreasing feedback frequency,
13 although becoming increasingly unrealistic in both structure and amplitude, until
14 1/30days when the intraseasonal fluctuations are overwhelmingly dominated by
15 unorganized small-scale perturbations in both atmosphere and ocean, as well as at the
16 atmosphere-ocean interface where heat and energy are rigorously exchanged. The main
17 conclusion is less frequent the SST feedback, more unrealistic the simulations. Our
18 results suggest that more spontaneous atmosphere-ocean interaction (e.g., ocean
19 response once every time step to every three days in this study) with high vertical
20 resolution in the ocean model is a key to the realistic simulation of the MJO and should
21 be properly implemented in climate models.

22

23 1. Introduction

24 The Madden-Julian Oscillation (MJO) is a large-scale tropical circulation that
25 propagates eastward from the tropical Indian Ocean (IO) to the western Pacific (WP)
26 with a periodicity of 30–80 days (Madden and Julian, 1972). In the Indo-Pacific region,
27 the MJO processes involve intraseasonal variability of sea surface temperature (SST)
28 (Chang et al., 2019; DeMott et al., 2014, 2015; Jiang et al., 2015, 2020; Krishnamurti

格式化: 字型色彩: 自動

格式化: 內文, 靠左, 縮排: 左: 0 公分, 第一行: 0 字元, 行
距: 單行間距, 貼齊格線

已刪除: the

30 et al., 1998; Li et al., 2014; Li et al., 2020a; Newman et al., 2009; Pei et al., 2018; Stan,
31 2018; Tseng et al., 2015). The tropical air–sea interaction, influenced by the upper ocean,
32 plays a crucial role in determining MJO characteristics due to the high heat capacity of
33 the upper ocean within the intraseasonal range, which acts as a significant heat source
34 for atmospheric variability (Watterson 2002; Sobel and Gildor 2003; Maloney and
35 Sobel 2004; Sobel et al. 2010; Liang and Du, 2022).

36 Analyzing the mechanism of the intraseasonal oscillation (ISO) reveals that heat
37 fluxes play a critical role in the development of intraseasonal SST variability (Hong et
38 al., 2017; Liang et al., 2018). As demonstrated in Fu et al. (2017), underestimation
39 (overestimation) of the air–sea coupling's impact on MJO simulations occurs when it is
40 weak (strong) in the intraseasonal SST variability. Simulation improvements in the
41 eastward propagation and regulation of MJO periodicity in the coupled models can be
42 attributed to several factors such as enhanced low-level convergence and convective
43 instability to the east of convection, as well as enhanced latent heat fluxes (Savarin and
44 Chen, 2022) and SST cooling to the west of convection (DeMott et al., 2014). SST
45 gradients have been found to induce patterns of mass convergence and divergence
46 within the marine boundary layer (MBL), initiating atmospheric convection (de Szoeké
47 and Maloney, 2020; Lambaerts et al., 2020).

48 Several recent studies have made significant progress in understanding the impact
49 of air–sea coupling on the MJO, particularly at sub-daily scales (e.g., DeMott et al.,
50 2015; Kim et al., 2018; Seo et al., 2014; Voldoire et al., 2022; Zhao and Nasuno, 2020).
51 However, there is relatively limited discussion on the effect of air–sea coupling from
52 few days to within half of the MJO period. Several studies have investigated the impact
53 of intraseasonal SST on the MJO by coupled or uncoupled models. (e.g., DeMott et al.,
54 2014; Gao et al., 2020b; Klingaman, and Demott, 2020; Pariyar et al., 2023; Stan, 2018).
55 Simulations using time-varying SSTs from coupled global climate model (CGCM) to

56 force the atmospheric general circulation model (AGCM) showed a reduced
57 intraseasonal SST variability, leading to weakened air–sea heat fluxes and eastward
58 propagation (DeMott et al., 2014; Gao et al., 2020b; Klingaman, and Demott, 2020;
59 Pariyar et al., 2023). Moreover, the absence of few days variability in SST promotes
60 the amplification of westward power associated with Rossby waves (Stan, 2018).

61 Incorporating two-way coupling between the ocean and atmosphere has been
62 proved valuable for simulating and predicting intraseasonal variability (e.g., DeMott et
63 al., 2014; Lan et al., 2022; Stan, 2018; Tseng et al., 2015, 2020). As demonstrated in
64 recent studies (e.g., Ge et al. 2017, Lan et al., 2022, Shinoda et al. 2021, and Tseng et
65 al. 2015, 2022), incorporating high vertical resolution near the ocean surface positively
66 influences the accurate representation of intraseasonal SST variability and enhances the
67 MJO prediction capabilities. However, how frequent is the coupling needed is still not
68 fully understood, considering the fact that the ocean and atmosphere could evolve in
69 distinct time scales. And, would the coupling frequency in numerical models influence
70 the accuracy of the MJO simulation?

71 In this study, we aim to investigate the specific effects of oceanic feedback
72 frequency (FF) through air–sea coupling on the atmospheric intraseasonal variability,
73 using the National Center for Atmospheric Research (NCAR) Community Atmosphere
74 Model 5.3 (CAM5.3) coupled with the single-column ocean model named Snow–Ice–
75 Thermocline (SIT). The coupled model is referred to as CAM5–SIT. The SIT model,
76 consisting of 41 vertical layers, enables the simulation of SST and upper-ocean
77 temperature variations with high vertical resolution (Lan et al., 2022). We have
78 demonstrated in previous studies that coupling the SIT significantly improved the MJO
79 simulations in several AGCMs (Tseng et al. 2015, 2022, Lan et al. 2022). The ability of
80 the SIT with extremely high-resolutions (i.e., 12 layers within the first 10.5 m) to well
81 resolve the upper ocean warm layer and the cool skin of the ocean surface was identified

82 as the main reason for the improved simulations.

83 The structure of this paper is organized as follows. Section 2 introduces the model,
84 data, methodology, and experiments employed in this study. The performance of the
85 CAM5–SIT models in simulating the MJO is discussed in Section 3, while Section 4
86 focuses on the impact of different configurations of sub-seasonal SST feedback
87 periodicity on MJO simulations. Finally, Section 5 presents the conclusions.

88

89 **2. Data, model experiments, and methodology**

90 **2.1 Observational data**

91 Observational data sets used in this study include precipitation from the Global
92 Precipitation Climatology Project (GPCP, 1° resolution, 1997–2010; Adler et al., 2003),
93 outgoing longwave radiation (OLR, 1° resolution, 1997–2010; Liebmann, 1996), and
94 daily SST (optimum interpolated SST, OISST, 0.25° resolution, 1989–2010; Banzon et
95 al., 2014) from the National Oceanic and Atmosphere Administration, and the fifth
96 generation ECMWF reanalysis (ERA5), with a resolution of 0.25° for the period of
97 1989–2020 (Hersbach and Dee, 2016). Various variables from ERA5 were considered,
98 including winds, vertical velocity, temperature, specific humidity, sea level pressure,
99 geopotential height, latent and sensible heat, and shortwave and longwave radiation.
100 For the initial conditions of the SIT, the SST data was obtained from the Hadley Centre
101 Sea Ice and Sea Surface Temperature dataset version 1 (HadISST1), with a resolution
102 of 1° for the period of 1982–2001 (Rayner et al., 2003). The ocean subsurface data,
103 including climatological ocean temperature, salinity, and currents in 40 layers, were
104 retrieved from the National Centers for Environmental Prediction (NCEP) Global
105 Ocean Data Assimilation System (GODAS) with a resolution of 0.5° for the period of
106 1980–2012 (Behringer and Xue, 2004). These data were used for a weak nudging
107 (Tseng et al. 2015 2022; Lan et al. 2022) in the SIT model.

108

109 **2.2 Experimental design**

110 In this study, we investigated the role of oceanic FF using coupled CAM5–SIT and
111 atmosphere-only CAM5 (A–CTL). Previous studies (Lan et al., 2022; Tseng et al., 2022)
112 have provided a detailed description of the every timestep coupling CAM5–SIT model
113 and its performance in simulating the MJO. Table 1 displays the experimental
114 configuration, incorporating monthly HadISST1 (uncoupled region) and ice
115 concentrations over a 30-year period centered around the year 2000 (F2000 compsets,
116 Rasch et al., 2019). Solar insolation, greenhouse gas and ozone concentrations, and
117 aerosol emissions representative of present-day conditions were prescribed. In the A–
118 CTL, observed monthly-mean SST around the year 2000 was prescribed to force the
119 CAM5. For the coupled simulations, we adjusted the Flux Coupler (CPL) restriction in
120 the Climate Earth System Model (CESM1; Hurrell et al., 2013) by implementing
121 asymmetric exchange frequencies between the atmosphere and the ocean. The ocean
122 continuously receives atmospheric forcing at every time step (30 minutes) and the
123 temperature changes accordingly, but the SST seen by the atmospheric model is fixed
124 at each timestep for a specified time span (e.g., 1, 3, 6, 12, 18, 24, and 30 days). That
125 is, the SST seen by the atmospheric model only changed until the end of the specified
126 time span.

127 Two sets of experiments in addition to the A–CTL were conducted, each
128 representing a different SST feedback frequency:

129 (1) High-frequency SST feedback set: This set includes the control experiment
130 (C–CTL) with SST feedback at every timestep (FF as 48/day), once a day (C–
131 1day: FF as 1/day), and every 3 days (C–3days: FF as 1/3days).

132 (2) Low-frequency SST feedback set: This set includes experiments with SST
133 feedback to the atmosphere for every 6 days (C–6days: FF as 1/6days), 12 days

134 (C–12days: FF as 1/12days), 18 days (C–18days: FF as 1/18days), 24 days (C–
135 24days: FF as 1/24days), and 30 days (C–30days: FF as 1/30days).

136 The SIT is coupled to CAM5 between 30° N to 30° S. The ocean was weakly
137 nudged (using a 30-day exponential time scale) between depths of 10.5 m and 107.8 m,
138 and strongly nudged (using a 1-day exponential time scale) below 107.8 m, based on
139 the climatological ocean temperature data from NCEP GODAS. No nudging was
140 applied in the upper-most 10.5 meters, allowing the simulation of rigorous air–sea
141 coupling near the ocean surface.

142 During the simulation, the SIT recalculated the SST within the tropical air–sea
143 coupling region. Outside this coupling region, the annual cycle of HadSST1 was
144 prescribed. No SST transition between the tropical air–sea coupling zone and the
145 extratropical SST-prescribed regions was applied. The ocean bathymetry for the SIT
146 was derived from the NOAA’s 1 arc-minute global relief model of Earth's surface that
147 integrated land topography and ocean bathymetry (ETOPO1) data (Amante and Eakins,
148 2009). To ensure consistency and comparability, all observational, atmospheric, oceanic,
149 and reanalysis data were interpolated into a horizontal resolution of $1.9^\circ \times 2.5^\circ$ for
150 model initialization, nudging, and comparison of experimental simulations.

151

152 **2.3 Methodology**

153 The analysis focused on the boreal winter period (November–April), the season
154 with the most pronounced eastward propagation of the MJO. To identify intraseasonal
155 variability, the CLIVAR MJO Working Group diagnostics package (CLIVAR, 2009)
156 and a 20–100-day filter (Wang et al., 2014) was used. MJO phases were defined based
157 on the Real-time Multivariate MJO series 1 (RMM1) and series 2 (RMM2) proposed
158 by Wheeler and Hendon (2004), which utilized the first two principal components of
159 combined near-equatorial OLR and zonal winds at 850 and 200 hPa. The band-pass

160 filtered data were used to calculate the index and define the MJO phases.

161 Analysis of column-integrated MSE budgets was conducted to investigate the
162 association between tropical convection and large-scale circulations. The column-
163 integrated MSE budget equation (e.g., Sobel et al., 2014) is approximately given by

$$164 \left\langle \frac{\partial h}{\partial t} \right\rangle' = - \left\langle u \frac{\partial h}{\partial x} \right\rangle' - \left\langle v \frac{\partial h}{\partial y} \right\rangle' - \left\langle w \frac{\partial h}{\partial p} \right\rangle' + \langle LW \rangle' + \langle SW \rangle' + \langle SH \rangle' + \langle LH \rangle' \quad (1)$$

165 where h denotes the moist static energy

$$166 h = c_p T + gz + L_v q \quad (2)$$

167 where T is temperature (K); q is specific humidity (Kg Kg⁻¹); c_p is dry air heat capacity
168 at constant pressure (1004 J K⁻¹ kg⁻¹); L_v is latent heat of condensation (taken constant
169 at 2.5×10^6 J kg⁻¹); u and v are horizontal and meridional wind (m s⁻¹), respectively; w
170 is the vertical pressure velocity (Pa s⁻¹); LW and SW are the longwave and shortwave
171 radiation flux (W m⁻²), respectively; and LH and SH are the latent and sensible surface
172 heat flux (W m⁻²), respectively. The angle bracket ($\langle * \rangle$) represents mass-weighted
173 vertical integration from 1000 to 100 hPa; and the intraseasonal anomalies are
174 represented as $\langle * \rangle'$.

175

176 3. Results

177 3.1 The mean state and intraseasonal variability of SST

178 The variability of SSTs plays a crucial role in the dynamics of the MJO. Studies
179 based on observations from TOGA COARE and DYNAMO revealed that MJO events
180 exhibited a stronger ocean temperature response compared to average conditions (de
181 Szoeke et al., 2014). Wu et al. (2021) revealed the better MJO prediction skill in the
182 CGCM could be contributed by the improved representation of high-frequency SST
183 fluctuations related to the MJO, with warm (cold) SST anomalies to the east (west) of
184 MJO convection, through the convection–SST feedback processes (Li et al., 2020a; Wu

185 et al., 2021). It is therefore necessary to check on the influences of coupling and coupling
186 frequency on the SST fluctuations.

187 Table 2 presents the oceanic temperature anomalies for the DJF seasonal mean,
188 including the differences in oceanic temperature between the SST and depths of 10m
189 ($\overline{\Delta T}_{0-10m}$) and 30m ($\overline{\Delta T}_{0-30m}$), as well as 20–100 days maximum and minimum SST
190 and oceanic temperature at 10m depth (T_{10m}). The region of 110–130° E and 5–15° S
191 was selected because of the largest variation in the 20–100-day bandpass-filtered SST
192 when the MJO passes over the Indo-Pacific region. Simulated DJF seasonal mean SST
193 (300.8K to 302.0 K) are generally smaller than OISST (302.2 K) but increase with the
194 lower SST feedback frequency except in C–30days (302.7 K), while the SST standard
195 deviation remains within 0.8 K, smaller than OISST (0.96 K), except in C–24days (1.06
196 K) and C–30days (1.71 K) that implies the potential jump in SST.

已删除:.)

197 The simulated subsurface (0–10m and 0–30m) ocean temperatures were compared
198 with those in the NCEP GODAS reanalysis and presented as ($\overline{\Delta T}_{0-10m}$ and $\overline{\Delta T}_{0-30m}$).
199 The $\overline{\Delta T}_{0-10m}$ in high-frequency experiments maintained 0.1 K temperature difference.
200 In low-frequency experiments, $\overline{\Delta T}_{0-10m}$ increased from 0.2 to 1.0 K with decreasing
201 SST feedback frequency. The temperature difference ($\overline{\Delta T}_{0-30m}$) in both high-frequency
202 and low-frequency experiments remains approximately 0.8K, except for C–24days and
203 C–30days with an increase as high as 1.4 K and 2.1 K, respectively, with larger standard
204 deviations. The comparison revealed the cooling effect of the SIT on the seasonal mean
205 SST, especially in the higher-frequency coupling experiment due to the more rigorous
206 heat exchanges between ocean and atmosphere. However, in the lower frequency
207 experiments, the SST became much warmer and so did vertical temperature differences
208 due likely to the unrealistically large heat accumulation of loss in the ocean.

已删除:.

209 As for the MJO simulation, the SST fluctuation is more relevant. The OISST
210 fluctuation through a MJO cycle was about ± 0.21 K. In comparison, the uncoupled A–

213 CTL, which was forced by monthly mean HadISST1, yielded a negligible SST
214 fluctuation (-0.003–0.02 K) as expected. In the high-frequency experiments, SST
215 fluctuated in magnitudes similar to that in the daily OISST. The amplitude became
216 unrealistically larger in the low-frequency coupling experiments with C–30days
217 reaching as high as 0.6 K. The increasingly larger amplitudes were likely resulted from
218 the heat accumulation in the ocean because of less frequent feedback (or heat release) to
219 the model atmosphere. Changes in coupling frequency led to different amplitudes of SST
220 fluctuation in a MJO cycle. As will be revealed latter, this effect had marked influence
221 on the MJO simulations.

222

223 **3.2 MJO simulation: high-frequency and low-frequency SST feedback experiments**

224 **3.2.1 General structure**

225 The propagation characteristics of the different experiments were analyzed using
226 the wavenumber-frequency spectrum (W-FS). The spectra of unfiltered U850 in ERA5,
227 A–CTL, and all coupling experiments with different feedback frequency are shown in
228 Fig. 1a–j. The C–CTL experiment accurately captures the eastward propagating signals
229 at zone wavenumber 1 with 30–80-day period (Fig. 1a and 1c), although with a slightly
230 larger amplitude than ERA5 (Fig. 1a). By contrast, the uncoupled A–CTL produced an
231 unrealistic spectral shift to time scales longer than 30–80 days (Fig. 1b) and simulated
232 the unrealistic westward propagation at wavenumber 2.

233 The W-FS spectra of the C–1day and C–3day experiment show two peaks for zone
234 wavenumber 1 over the 30 to 80-day period. The low-frequency experiments (i.e., from
235 C–6days to C–30days) increasingly enhanced the amplitudes and lowered the
236 frequency of intraseasonal perturbations with decreasing feedback frequency.
237 Furthermore, unrealistic westward W-FS of U850 becomes evident in (Fig. 1h–i) in the

238 C–18days, C–24days, and C–30days experiments, reflecting the stationary nature of
239 simulated MJO [seen in Fig. 2i–j](#).

240 The Hovmöller diagrams in Fig. 2a–j depict the evolution of 10° N–10° S averaged
241 precipitation and U850 anomalies on intraseasonal timescales, represented by the
242 lagged correlation coefficients with the precipitation averaged over 10° S–5° N, 75–
243 100° E. In GPCP/ERA5, observed precipitation and U850 propagated eastward from
244 the eastern IO to the dateline, with precipitation leading U850 by approximately a
245 quarter of a cycle and a propagation speed of about 5 m s⁻¹ (Fig. 2a). The A–CTL
246 simulation was dominated by stationary features, with westward-propagating tendency
247 over the IO and weak and slow eastward propagation over the MC and WP (Fig. 2b).
248 The Hovmöller diagrams derived from high-frequency and low-frequency experiments
249 (Fig. 2c–h) display the key eastward propagation characteristics in both precipitation
250 and U850, as well as the phase relationship between them, except in C–24days and C–
251 30days that were dominated by stationary perturbations. Further decreased feedback
252 frequency from 1/C–24days to 1/C–30days also further weakened the signals of
253 precipitation and U850. More detailed discussion on this topic will be presented in the
254 subsequent chapter.

255 We conducted a wavenumber-frequency power spectral analysis (Wheeler and
256 Kiladis 1999) to examine the phase lag and coherence between the tropical circulation
257 and convection. Figures 3a–i illustrate the symmetric part of OLR and U850 for
258 NOAA/ERA5 data and all model experiments. The MJO band exhibits a high degree
259 of coherence, indicating a strong correlation between NOAA MJO-related OLR signal
260 and wavenumbers 1–3 (Fig. 3a). The phase lag in the 30–80-day band is approximately
261 90°, consistent with previous studies (Ren et al., 2019; Wheeler and Kiladis 1999). All
262 model experiments simulated the coherence within wavenumber 3 in the MJO band,
263 with a phase lag similar to NOAA/ERA5 data. However, the A–CTL spectrum exhibits

264 only half of the observed coherence peak at wavenumber 1, and also weaker coherence
265 at wavenumbers 2–3 for the 30–80-day period compared to NOAA/ERA5 data. The
266 experiments C–CTL, C–1day, C–3days, C–6days, C–12days, and C–18days yielded
267 wavenumber-1 coherence peak similar to that in NOAA/ERA5. Additionally, as the
268 SST feedback frequency decreases from 1/12days to 1/30days, the experiments
269 increasingly simulated unrealistic coherence in the very low frequency with a wide
270 range of zonal wavenumber from 1 to 12 (Fig. 3g–j), i.e., no zonal scale preference.

271 Figure 4 shows the phase–longitude diagrams in which the 20–100-day filtered
272 precipitation (shaded) and SST (contour) anomalies were averaged over 10° S to 10° N
273 to determine the relationship between precipitation and SST fluctuations and to provide
274 insights into the connection between air–sea coupling and convection. As expected, the
275 A–CTL did not simulate the eastward-propagating coupled SST-convection
276 perturbations as in observation (Fig. 4a), whereas C–CTL, C–1day, and C–3days
277 properly reproduced the observed features. The eastward-propagating coupled
278 perturbations were also simulated in C–6days, C–12days, and C–18days, but with
279 unrealistically increasing amplitudes near the dateline, especially in the C–18days
280 experiment. The perturbation amplification near the dateline was likely due to the lack
281 of ocean circulation in the CAM5–SIT. The amplification was also seen in C–24days
282 that failed to simulate the eastward-propagating intraseasonal perturbations. When
283 coupling frequency was reduced to 1/30days, the eastward propagation could no longer
284 be simulated and was replaced by unorganized standing oscillations in much smaller
285 zonal scales.

286 Liang et al. (2018) suggested that SST leading precipitation by 10 days implies
287 air–sea interactions at the intraseasonal timescale during MJO events, with SST playing
288 a crucial role in modulating the MJO's intensity and propagation. The A–CTL
289 simulation exhibited weak SST anomalies and stationary precipitation when using the

290 monthly average HadISST1. By contrast, the C–24days and C–30days experiment
291 showed no clear phase lag between disorganized SST and precipitation perturbations.

292 A comparison between simulation results and observation indicates that the air–sea
293 interaction plays a crucial role in facilitating eastward propagation and higher frequency
294 feedback yields more realistic simulations.

295

296 3.2.2 Vertical structures of the MJO in the atmosphere

297 Air–sea interaction plays a significant role in influencing atmospheric moisture and
298 convection associated with the MJO (Savarin and Chen, 2022). Whereas the ocean to
299 the east of deep convection warmed due to more downwelling shortwave radiation and
300 less heat fluxes into the atmosphere associated with weaker winds, near-surface
301 moisture convergence under the anomalous subsidence over the warmer water
302 preconditioned the eastward movement of the deep convection (DeMott et al., 2015;
303 Zhang, 2005). The MJO was noted to detour southward when crossing the MC region,
304 exhibiting enhanced convective activity preferentially in the southern MC area and
305 weaker convection in the central MC area (Hsu and Lee 2005, Wu and Hsu 2009, and
306 Kim et al. 2017). Hovmöller diagrams in Fig. 5a–j illustrate the relationship between
307 the vertical structure of air temperature (contoured, in K) and specific humidity
308 (shading, in g kg^{-1}) anomalies from the surface to 200 hPa averaged over 5–20° S and
309 120–150° E. In ERA5, the lower-level positive temperature anomaly in phase 3 (i.e.,
310 preconditioning phase) leads the development of deep temperature and moisture
311 anomalies (i.e., deep convection) after phase 4 over the MC, when moisture anomalies
312 reached the maxima at 700–500 hPa. This two-phase upward development was not
313 properly simulated in A–CTL, which shows sudden switch between positive and
314 negative anomalies in the entire troposphere, instead of progressively upward
315 development with time. The upward development was generally simulated in coupled

316 simulations from C-CTL to C-6days (Fig. 5c-e), although the negative temperature
317 anomalies below 500 hPa were over-simulated after phase 5. It became less well
318 simulated beyond C-12days and was gradually replaced by sudden phase switch as in
319 the A-CTL, especially in C-30days (Fig. 5f-j). The preconditioning phase completely
320 disappears in C-18 days and beyond. As identified in previous studies, the two-phase
321 upward development is a manifestation of air-sea coupling. The missing of this
322 coupling evidently resulted in the poor simulation in the A-CTL and extremely low
323 feedback frequency experiments.

已删除:-

已删除:-

324

325 3.2.3 Vertical structures of the MJO in the ocean

326 The 1-D turbulence kinetic energy (TKE) ocean model incorporates a high vertical
327 resolution that captures the vertical gradient of temperature in the upper ocean. Figure
328 6 (left column) illustrates the vertical structures of oceanic temperature between 0- and
329 60-meters during phase 2-3 when the deep convection occurred over the eastern IO
330 (60-90° E) and easterly anomalies prevailed over the MC and western Pacific. In the
331 high-frequency experiments (Fig. 6a, 6c, 6e), the upper oceanic temperatures exhibit
332 warming patterns within 30 meters depth at 100-140° E (i.e., east of the deep
333 convection and under the easterly anomalies), apparently due to more downwelling
334 short wave radiation and less heat flux release to the atmosphere. By contrast, the
335 cooling near the dateline was associated with westerly anomalies. With decreasing
336 feedback frequency, the cooling to the east of 150°E seen in high frequency experiments
337 was replaced by oceanic warming that amplified with further feedback frequency
338 decrease. The warming region that became more widespread and larger amplitude with
339 less frequent feedback eventually grew to cover the entire IO and WP, an area much
340 larger than the scale of the atmospheric MJO. The mismatch between the atmospheric
341 and oceanic anomalies suggested the weakening atmospheric-ocean coupling that

344 resulted in poor simulation of the MJO in the low frequency feedback simulations. The
345 emergence of small-scale unorganized structures with decreasing feedback frequency
346 is also evident in phase 4-5 (right column of Fig. 6), e.g., negative ocean temperature
347 anomalies in the Indian Ocean under the prevailing westerly anomalies.

348

349 **4. Discussion**

350 **4.1 Dynamic lead-lag relationship in intraseasonal variability**

351 The lead-lag relationship refers to a situation where one variable (leading) is
352 cross-correlated with the values of another variable (lagging) in subsequent phases,
353 particularly in the case of SST fluctuations and MJO-related atmospheric variations
354 between phase 1 and 8 within the domain of 110–130° E and 5–15° S (Fig. 7). The
355 analyzed variables include 20–100-day filtered latent heat flux (LHF, indicated by green
356 shading), OLR (indicated by a yellow bar chart), net surface solar radiation (FSNS,
357 indicated by an orange bar chart), U850 (indicated by a purple bar chart), 30-meter
358 depth oceanic temperature (30-m T multiplied by 100, indicated by a black line), and
359 SST (multiplied by 10, indicated by an orange line). Positive value in LHF and FSNS
360 represents an upward flux from ocean to atmosphere.

361 Decrease in LHF, which indicates a reduction in heat loss from the ocean, and
362 negative FSNS, indicating that solar radiation is heating the ocean, coincide with
363 easterly anomaly that contributes to positive SST anomaly in ERA5 (Fig. 7a). Reversed
364 fluxes are associated with westerly anomalies. This lead-lag relationship depicts the in-
365 situ atmospheric forcing on the oceanic variability during a MJO. As the MJO
366 convection progresses through the region (110–130° E and 5–15° S), several changes
367 in atmospheric and oceanic variables occur. These changes include a shift in OLR from
368 positive to negative values, a decrease in SST, a transition to westerly winds, and an
369 increase in positive FSNS and LHF (Fig. 7a). The temporal variations in SST anomaly

370 from C-CTL to C-12days were predominantly influenced by FSNS, with LHF playing
371 a secondary role, similar to the findings of Gao et al. (2020a). With the exception of
372 experiments of A-CTL, C-24days, and C-30days, both the high-frequency and low-
373 frequency SST feedback experiments simulated similar lead-lag relationships as in
374 ERA5 (Fig. 7c-h). In the C-24days and C-30days experiments, LHF was the largest
375 flux term (note the different vertical scale for the two experiments) whereas the wind,
376 OLR, and FSNS anomalies were much weaker than in other experiments. In the A-CTL
377 experiment, which was forced by monthly HasSST1 data, the SST anomalies were
378 small as expected, whereas fluxes although weak are still evident in response to
379 atmospheric perturbations (Fig. 7b). Conversely, in both C-24days and C-30days
380 experiments, a misalignment in the lead-lag relationship was observed, accompanied
381 by weak anomalies in OLR and FSNS. (Fig. 7i and 7j). This disparity between LHF and
382 wind was likely due to the unrealistically widespread and large oceanic warming as
383 shown in Fig. 6m and 6o.

384 In the simulations, the maximum positive anomaly in 30-m T was delayed by one
385 phase compared to SST, indicating the transfer of heat from the ocean surface into the
386 upper ocean progressively. Similarly, the occurrence of the most negative 30-m T
387 anomaly was also delayed by one phase compared to SST, revealing the buffering role
388 of the upper ocean when the atmospheric component of the MJO extracted (or deposited)
389 heat (energy) from (in) the ocean (Fig. 7c-i). This delayed effect was also evident in
390 the field campaign. de Szoeke et al. (2015) observed that the warmest 10-m ocean
391 temperature occurred a few days later than the peak temperature at 0.1 m. Additionally,
392 the 0.1-m ocean temperature was typically as warm as or warmer than the 10-m
393 temperature as seen in Fig. 6. In the extreme low frequency feedback experiments, the
394 amplitude of 30-m temperature became unrealistically large due likely to the continuous
395 accumulation or loss of the ocean heat.

396

397 4.2 Unorganized perturbations in extreme frequency feedback scenarios

398 DeMott et al. (2014) noted that in uncoupled experiments, the NCAR CAM
399 superparameterized version 3 (SPCAM3) exhibited strong eastward propagation when
400 5-day running mean SST was prescribed, but relatively weaker propagation for monthly
401 mean SST. This raises the question of how much SST feedback periodicity is necessary
402 to maintain robust eastward propagation in coupled experiments. This tendency was
403 also seen in our study, that is, slower propagation (or weaker tendency) with decreased
404 feedback frequency until the C-24days experiment (Figs. 1-7). By 1/30days, the
405 perturbations became stationary.

406 Generally, C-18days exhibited the unrealistic overestimation of intraseasonal
407 variability while maintaining eastward propagation of the MJO. Here, we are not
408 suggesting that C-18days represents the optimal SST feedback experiment. Figure 8
409 highlights the considerable differences in the simulation of MJO perturbations at phase
410 2-3 between C-18days and C-30days experiments. In C-18days, negative OLR
411 anomalies were widespread from the western IO to the MC, while in reality it should
412 be observed mainly in the IO and be accompanied by positive anomalies in the eastern
413 MC, i.e., a west-east dipolar structure (Fig. 8a). In C-30days, the OLR anomaly,
414 although was still the dominant feature in the Indian Ocean-western Pacific region,
415 became much weaker and characterized by smaller scale perturbations. These OLR
416 anomalies were generally associated with upper-level convergence (not shown)
417 embedded in much weaker wind anomalies (U200) compared to those in C-18days.
418 The circulation and OLR in C-24days exhibited the characteristics similar to those in
419 C-18days but with the OLR anomalies breaking up into smaller scales.

420 Furthermore, in the C-18days and C-24days experiments, negative anomalies
421 indicative of a downward direction in LHF and net surface heat flux (Fig. 8d, 8e, 8g,

已删除: in

已删除: Indian Ocean

已删除: Indian Ocean

已删除: positive

426 and 8h), were predominantly observed in the convection-inactive region to the east of
427 150°E where low-level easterly wind and positive SST anomalies prevailed (Fig. 8j and
428 8k). The OLR, winds, heat fluxes, and SST to the west of 150°E exhibited similar
429 correspondences between variables but in opposite phase. With feedback frequency
430 reduced to 1/30days (Fig. 8f, 8i, and 8l), the heat fluxes and SST anomalies broke into
431 unorganized smaller scale features, consistent with the ocean temperature jump shown
432 in Fig. 6h. Although the wind fields in the both upper and lower levels were still
433 characterized by large-scale structure, the corresponding divergence were dominated
434 by much smaller scale perturbations (not shown), similar to heat fluxes and SST. The
435 increasingly dominant smaller scale perturbations can also be inferred from Fig. 2h-j
436 and 4h-j. In addition, the large power spectra in the low frequency band spread across
437 a wide range of wavenumbers, reflecting the smaller scale nature of the simulated
438 perturbations in C-30days (Fig. 3j). This disparity between the scale of rotational and
439 divergent winds suggests that the poor coupling between the convection and large-scale
440 circulation.

已删除:)

已删除: negative

441 With decreased feedback frequency of SST from C-CTL to C-30days, the ocean
442 continued to receive atmospheric forcing, but the feedback response was delayed,
443 leading to the accumulation or loss of energy (temperature) in the upper ocean, as seen
444 in the SST distribution in the WP (Fig. 6 and 8). Subsequently, the C-30days
445 experiment exhibited comprehensive disorder over the Indo-Pacific region, with the
446 SST anomalies showing an unrealistically erratic spatial distribution characterized by
447 sudden jumps (Fig. 8l) associated with plus-minus latent heat flux and 10m wind
448 anomalies (Fig. 8f), net surface heat flux, and solar radiation (Fig. 8i). As a result, the
449 organized large-scale circulation seen in the MJO was not manifested. To this extreme,
450 the air-sea interaction observed in the MJO no longer worked properly in the model.

已删除: 3h-j

已删除: exhibiting a perturbed

451

456 4.3 Moist static energy (MSE) budget analysis

457 We diagnosed the relative contribution of each term in Eq. (1) to the MSE tendency
458 with a focus on the second (pre-conditioning) and fifth (convection crossing the MC)
459 phases. Figure 9 illustrates the physical processes associated with each term (averaged
460 over 10°S – 0° , 120 – 150°E) contributing to the column-integrated MSE tendency
461 ($\langle \text{dmdt} \rangle$) in Eq. (1) during phase 2 in ERA5 and model simulations. In ERA5, when
462 the MJO convection was in the eastern Indian Ocean, the column-integrated vertical
463 and horizontal advection ($-\langle \text{wdmdp} \rangle$ and $-\langle \text{vdm} \rangle$) over the MC area were the dominant
464 terms in the MSE budget and largely compensated by longwave radiation and latent
465 heat flux, as reported in Wang and Li (2020) and Tseng et al. (2022). All experiments
466 simulated the positive and negative contributions similar to those derived from ERA5
467 although with different amplitudes. Notably, the C–24days and C–30days simulated
468 relatively weak vertical advection and too strong negative latent heat flux and too weak
469 longwave radiation flux. As a result, the C–24days and C–30days simulated relatively
470 weak tendency compared to other experiments. The results are consistent with the poor
471 simulation of the MJO in the extreme low frequency feedback experiments discussed
472 above.

473 We compared the spatial distribution of column-integrated MSE tendency $\langle \text{dmdt} \rangle$
474 (shading), precipitation (contours), and 850-hPa wind (vectors) during phase 5, i.e., the
475 period when the strongest convection crossing the MC (Fig. 10). In ERA5, the main
476 convection (indicated by positive precipitation anomaly) is accompanied by low-level
477 convergence in the 850-hPa wind across the MC extending into the WP (Fig. 10a). A
478 positive $\langle \text{dmdt} \rangle$ is observed to the east of the MJO convection to the south of the
479 equator (Fig. 10a). Conversely, a negative tendency is observed to the west of the MJO
480 convection accompanied by negative precipitation anomalies further to the west. The
481 phase relationship between the MSE tendency and precipitation reflects the eastward-

482 propagating nature of the MJO. With the exception of A-CTL, C-24days, and C-
483 30days, the model simulations displayed a similar structure in the 20-100-day filtered
484 <dmdt>, precipitation, and 850-hPa wind vectors (Fig. 10c-h). although the exact
485 locations may be shifted compared to those derived from ERA5. The C-CTL simulated
486 relatively weak signals compared to ERA5, whereas the signals became increasingly
487 stronger with decreasing feedback frequency. The signals became unrealistically strong
488 beyond 1/18days feedback frequency and the lead-lag relationship between the MSE
489 tendency and precipitation became less clear. For example, positive precipitation
490 anomaly became in phase with the tendency in the western Pacific south of the equator
491 in C-24days and C-30days experiments, and the tendency was much weaker in C-
492 30days. The results were consistent with the weaker eastward propagation tendency in
493 the low-frequency feedback experiments, especially in C-24days and C-30days when
494 the feedback frequency became unrealistically low.

495 The corresponding MSE budget during phase 5 is shown in Fig. 10. The MC
496 has been identified as a barrier to the eastward propagation of the MJO (Hsu and Lee,
497 2005, Wu and Hsu 2009, Tseng et al. 2017, Li et al., 2020b) and approximately 30-50%
498 of the MJO experienced stalling over the MC (Zhang and Han, 2020). To determine
499 whether the MJO has sufficient energy to traverse the MC, we focused the analysis on
500 phase 5. Figure 11 illustrates the projection of each MSE component and decomposition
501 of the horizontal MSE advection at phase 5 over the MC region (20° S-20° N, 90-
502 210° E) following the approach of Tseng et al. (2022) and Jiang et al. (2018), where
503 F_s is total surface fluxes including SH and LH, and Q_f is vertically integrated net SW
504 and LW radiation. Unlike in phase 2 when vertical advection is the dominant term, the
505 MSE tendency was dominated by the horizontal MSE advection -<vdm> in ERA5 and
506 all experiments, except the A-CTL. This contribution increased with decreasing SST
507 feedback frequency. The weaker positive vertical advection -<wdmdp> did not vary

508 systematically with decreasing feedback frequency and even turned negative in C-
509 24days and C-30days. F_s and Q_r acted to damp the tendency by cancelling out the
510 effect of the advection term. F_s tended to be more negative with decreasing feedback
511 frequency and became much larger in C-30days. By contrast, Q_r was unrealistically
512 weak in C-18days, C-24days, and C-30days. The uncoupled simulation yielded much
513 weaker amplitude in all terms as expected.

514 The $\langle v_{dm} \rangle$ that contributed most to the eastward propagation of the MJO in
515 phase 5 was further decomposed into zonal ($\langle u_{dmx} \rangle$) and meridional ($\langle v_{dm} \rangle$)
516 components to examine their relative effects (Fig. 11). Both components contributed
517 positively, but the $\langle v_{dm} \rangle$ exhibited a larger amplitude, consistent with Tseng et al.
518 (2014, 2022). The $\langle v_{dm} \rangle$ of high-frequency SST feedback experiments yielded
519 results closely similar to ERA5. Comparatively, the $\langle v_{dm} \rangle$ term in low-frequency
520 SST feedback experiments (C-18days, C-24days, and C-30days) became
521 unrealistically large with decreasing feedback frequency, and the potential jump in SST.

已删除: .

522 Spatial distributions of $\langle w_{dmp} \rangle$, $\langle v_{dm} \rangle$, and 200-hPa wind at phase 5 are
523 shown in Fig. 12. In ERA5, the wind divergence at 200 hPa at phase 5 (Fig. 12a),
524 overlaid the 850-hPa convergence (Fig. 10a), reflecting a deep convection structure.
525 The model simulations exhibited a similar structure to ERA5 except in A-CTL, C-
526 24days, and C-30days experiments, and again the amplitude increased with decreasing
527 feedback frequency. In ERA5, negative $\langle w_{dmp} \rangle$ and $\langle v_{dm} \rangle$ anomalies (Fig. 12a)
528 were observed to the west of the MJO convection (Fig. 10a). The spatial distribution of
529 the negative $\langle v_{dm} \rangle$ anomaly (dashed-red contours) extends from the IO to the MC
530 and positive anomaly (predominantly meridional advection from the south, not shown)
531 in the western-central Pacific south of the equator tends to facilitate the eastward
532 propagation of deep convection in the western Pacific, consistent with Tseng et al.
533 (2014, 2022). The $\langle w_{dmp} \rangle$ with negative and positive anomaly to the west and east

已删除:-

535 of the deep convection also contributes to the eastward propagation of the MJO, but
536 with weaker contribution than $\langle vdm \rangle$. Again, these characteristics were not simulated
537 in A-CTL, whereas the amplitudes of both terms became increasingly larger with
538 decreasing feedback frequency until becoming unrealistically large beyond 1/18days.
539 In C-30days experiment both terms exhibited unorganized spatial structure as shown
540 in preceding discussion. In summary, the high-frequency feedback experiments
541 simulated an approximately 80% projection of $\langle vdm \rangle$ in ERA5, whereas the low-
542 frequency SST feedback experiments overestimated $\langle vdm \rangle$ anomalies (Fig. 12f-h).

543

544 5. Conclusions

545 This study built upon the work of Lan et al. (2022) and Tseng et al. (2022) by
546 coupling a high-resolution 1-D TKE ocean model (the SIT model) with the CAM5, i.e.,
547 a CAM5-SIT configuration, to investigate the effects of intraseasonal SST feedback on
548 the MJO. We introduced asymmetric exchange frequencies between the atmosphere and
549 the ocean, ensuring bidirectional interaction at each timestep within the experimental
550 periodicity by fixing the SST value in the coupler. This allowed us to create SST
551 feedback with various intervals at 30 minutes, 1, 3, 6, 12, 18, 24, and 30 days.

552 The aim is to assess the effect of SST feedback frequency, namely, how often
553 should the atmosphere-driven SST change feedback to the atmosphere and whether
554 there is a limit. With the exception of the C-24days and C-30days experiment, both the
555 high-frequency and low-frequency experiments demonstrated realistic simulations of
556 various aspects of the MJO when compared to ERA5, GPCP, and OISST data, although
557 the simulation results becoming increasingly amplified and unrealistic with decreasing
558 feedback frequency. These aspects included intraseasonal periodicity (Fig. 1), eastward
559 propagation (Fig. 2 and 4), coherence in the intraseasonal band (Fig. 3), tilting vertical
560 structure (Fig. 5), intraseasonal SST (Table 2) and oceanic temperature variances (Fig.

562 6), the lead–lag relationship of intraseasonal variability (Fig. 7), contribution of each
563 term to the column-integrated MSE tendency at the preconditioning phase (phase 2)
564 and mature phased (phase 5) (Fig. 9 and Fig. 11). The MSE tendency term was
565 dominated by the horizontal and vertical MSE advection in phase 5 and phase 2,
566 respectively, in ERA5 and most experiments. Furthermore, we deliberately extended
567 the SST feedback interval to an unrealistically long 30 days to investigate the limits of
568 delayed ocean response. The main conclusion is less frequent the update, more
569 unrealistic the simulation result.

570 The lead–lag relationship provides a visual representation of the variations in 20–
571 100-day filtered LHF, FSNS, OLR, U850 and SST with positive SST anomaly leading
572 the onset of the MJO convection (Fig. 7). This relationship highlights the
573 interconnected nature of surface heat fluxes, solar radiation, and atmospheric
574 circulation patterns, underscoring their mutual influence and interplay through air–sea
575 interaction. Our results indicate that the high-frequency (low-frequency) SST
576 experiments tended to underestimate (overestimate) the MJO simulation in CAM5–SIT
577 model. Whether this finding can be applied to other models warrants further
578 investigations.

579 The result of C–3days experiment is consistent with Stan (2018), suggesting the
580 absence of 1–5-day variability in SST would promote the amplification of westward
581 power associated with tropical Rossby waves. By comparing with the control
582 experiment in which SST feedback occurs at every time step (30 minutes), the C–1day
583 experiment (SST feedback once daily) confirmed the findings of Hagos et al. (2016)
584 and Lan et al. (2022) that the removal of the diurnal cycle would enhance the MJO. The
585 increasing feedback periodicity of SST in low-frequency experiments led to the
586 accumulation of atmospheric influences through short-wave and long-wave radiations
587 and surface heat fluxes, resulting in an unrealistically large ocean temperature

588 anomalies and variances within few tens of meters below ocean surface (Table 2). The
589 large-scale nature of the MJO remains intact with decreasing feedback frequency,
590 although becoming increasingly unrealistic in both structure and amplitude, until
591 1/30days when the intraseasonal fluctuations were overwhelmingly dominated by
592 unorganized small-scale perturbations in both atmosphere and ocean, as well as at the
593 atmosphere-ocean interface where heat and energy were rigorously exchanged.

已删除:

594 The reason causing the sudden change between C-24days and C-30days is not
595 entirely clear. Two possibilities are discussed here. The first possible reason leading to
596 this disorder is that when the ocean feedback is delayed for as long as 30 days (more
597 than half of the MJO period) both positive and negative fluxes would contribute to the
598 heat accumulation or loss in the ocean because of the MJO phase transition and result
599 in unorganized small scale structures in ocean temperatures, which could in turn affect
600 the heat flux and convection. The second possible reason would be that the SST
601 variation in a MJO event become more abrupt and may disrupt the large-scale nature of
602 the MJO into disorganized spatial distribution in atmosphere, ocean, and the interface
603 where rigorous heat exchange occurs. This disrupting effect of abrupt SST variation,
604 which is not explored in this study, warrants further studies with purposely designed
605 experiment to untangle.

已删除: change

已删除: . However, whether large-amplitude

已删除: fluctuations would induce unorganized small-scale perturbation

已删除: debatable. As seen in many hypothetic (or theoretical) studies, a sudden initiation of SST (or step-function like) could induce large scale responses. This issue remains an open question that

606 Finally, results of intraseasonal SST feedback experiments on MJO are
607 summarized schematically in Fig. 13, following DeMott et al. (2014). These
608 experiments included the uncoupled experiment (A-CTL), high-frequency SST
609 experiments (C-CTL, C-1day, and C-3days), low-frequency SST experiments (C-
610 6days, C-12days, C-18days), and extreme low-frequency experiment (C-24days and
611 C-30days). In the absence of intraseasonal SST variability, the eastward propagation of
612 the MJO was disrupted, leading to weakened or fragmented MJO activity as shown in
613 Fig. 13a. On the other hand, the high-frequency SST experiments closely mimicked

623 air-sea interaction and well captured the characteristics of the MJO. The time-varying
624 SSTs in the coupled simulation provided a certain degree of organization and sufficient
625 surface fluxes, which facilitated the development of the MJO circulation as illustrated
626 in Fig. 13b. The horizontal moist static energy tendency derived from increased low-
627 level convergence, especially due to the meridional advection of MSE, intensified the
628 MJO convection and triggered the eastward propagation over the MC region. The PBL
629 convergence ahead of the MJO convection is due to Kelvin-wave dynamics (Jiang,
630 2017), in conjunction with the background zonal flow structure (Tulich and Kiladis,
631 2021). Horizontal MSE or moisture advection in the lower troposphere, particularly the
632 seasonal mean low-level MSE influenced by the MJO's anomalous winds, has had a
633 significant impact on the MJO propagation. (Gonzalez and Jiang, 2017; Jiang, 2017).
634 This simulation result is consistent with the understanding that the MJO is primarily
635 attributed to the interaction between organized convection and large-scale circulations
636 that triggers the eastward propagation. As feedback frequency become lower, the major
637 characteristics of the MJO could still be simulated as depicted in Fig. 13c, but with
638 overestimated amplitudes and deteriorating simulations in spatial structures. In the
639 extreme low frequency experiments with frequency decreasing to 1/24days and
640 1/30days, unorganized structures started to emerge and broke up into smaller scale
641 perturbations as shown in Fig. 13d, when large-scale air-sea interaction embedded in
642 the MJO did not operate properly in the model. Eventually in the C-30days experiment,
643 unrealistically and spatially scattered anomalies in precipitation, jumping SST, surface
644 heat fluxes, and vertical and horizontal MSE advection became dominant features. All
645 these findings led to the major conclusion of this study: more spontaneous atmosphere-
646 ocean interaction (e.g., ocean response once every time step to every three days in this
647 study) with high vertical resolution in the ocean model is a key to the realistic
648 simulation of the MJO and should be properly implemented in climate models.

已删除: proper

已删除: proper

已删除: in the

652

653 *Code and data availability.* The model code of CAM5–SIT is available at
654 <https://doi.org/10.5281/zenodo.5510795>. Input data of CAM5–SIT using the
655 climatological Hadley Centre Sea Ice and Sea Surface Temperature dataset and
656 GODAS data forcing, including 30-year numerical experiments, are available at
657 <https://doi.org/10.5281/zenodo.5510795>.

658

659 *Author contributions.* YYL is the CAM5–SIT model developer and writes the majority
660 part of the paper. HHH contributes to the physical explanation and the reorganization
661 and revision of the manuscript. WLT assists in the MSE analysis.

662

663 *Competing interests.* The authors declare that they have no conflict of interest.

664

665 *Acknowledgements.* The contribution from YYL, HHH, and WLT to this study is
666 supported by the Ministry of Science and Technology of Taiwan under MOST 110-
667 2123-M-001-003, MOST 110-2811-M-001-603, MOST 109-2811-M-001-624 and
668 MOST108-2811-M-001-643. Our deepest gratitude goes to the editors and anonymous
669 reviewers for their careful work and thoughtful suggestions that have helped improve
670 this paper substantially. We sincerely thank the National Center for Atmospheric
671 Research and their Atmosphere Model Working Group (AMWG) for release
672 CESM1.2.2. We thank the computational support from National Center for High530
673 performance Computing of Taiwan. Thanks, ChatGPT for correcting the English
674 grammar.

675

676 **Reference**

677 Adler, R. F., Huffman, G. J., Chang, A., Ferraro, R., Xie, P.
678 P., Janowiak, J., Rudolf, B., Schneider, U., Curtis, S., Bolvin,

- 679 D., Gruber, A., Susskind, J., Arkin, P., and Nelkini, E.: The Version
680 2.1 Global Precipitation Climatology Project (GPCP) Monthly
681 Precipitation Analysis (1979 -Present), *J. Hydrometeor.*, 4(6), 1147-
682 1167, [https://doi.org/10.1175/1525-
683 7541\(2003\)004<1147:TVGPCP>2.0.CO;2](https://doi.org/10.1175/1525-7541(2003)004<1147:TVGPCP>2.0.CO;2), 2003.
- 684 Amante, C., and Eakins, B. W.: ETOPO1 1 arc-minute globe relief model:
685 Procedures, data sources and analysis, NOAA Tech. Memo. NESDIS
686 NGDC-24, NOAA, Silver Spring, MD, 19 pp.,
687 <https://doi.org/10.7289/V5C8276M>, 2009.
- 688 Banzon, V. F., Reynolds, R. W., Stokes, D., and Xue, Y.: A 1/4-spatial-
689 resolution daily sea surface temperature climatology based on a
690 blended satellite and in situ analysis, *J. Climate*, 27, 8221–8228,
691 <https://doi.org/10.1175/JCLI-D-14-00293.1>, 2014.
- 692 Behringer, D. W., and Xue, Y.: Evaluation of the global ocean data
693 assimilation system at NCEP: The Pacific Ocean. Eighth Symposium
694 on Integrated Observing and Assimilation Systems for Atmosphere,
695 Oceans, and Land Surface, AMS 84th Annual Meeting, Washington
696 State Convention and Trade Center, Seattle, Washington, 11-15.
697 Derber, J.C., and A. Rosati, 1989: A global oceanic data assimilation
698 system, *J. Phys. Oceanogr.*, 19, 1333–1347,
699 <https://ams.confex.com/ams/pdfpapers/70720.pdf>, 2004.
- 700 Chang, M.-Y., Li, T., Lin, P.-L., and Chang, T.-H.: Forecasts of MJO
701 Events during DYNAMO with a Coupled Atmosphere-Ocean Model:
702 Sensitivity to Cumulus Parameterization Scheme, *J. Meteorol.*
703 *Res.*, 33, 1016–1030, <https://doi.org/10.1007/s13351-019-9062-5>,
704 2019.
- 705 CLIVAR MADDEN–JULIAN OSCILLATION WORKING GROUP: MJO
706 simulation diagnostics, *J. Climate*, 22, 3006–3030,
707 <https://doi.org/10.1175/2008JCLI2731.1>, 2009.
- 708 DeMott, C. A., Klingaman, N. P., and Woolnough, S. J.: Atmosphere-
709 ocean coupled processes in the Madden-Julian oscillation, *Rev. of*
710 *Geophysics*, 53, 1099– 1154, [https://doi.org/10.1002/2014RG00047
711 8](https://doi.org/10.1002/2014RG000478), 2015.
- 712 DeMott, C. A., Stan, C., Randall, D. A., and Branson, M.
713 D.: Intraseasonal variability in coupled GCMs: The roles of ocean
714 feedbacks and model physics, *J.*
715 *Climate*, 27(13), 4970– 4995. [https://doi.org/10.1175/JCLI-D-13-
716 00760.1](https://doi.org/10.1175/JCLI-D-13-00760.1), 2014.
- 717 de Szoek, S. P., Edson, J. B., Marion, J. R., Fairall, C. W., and Bariteau,
718 L.: The MJO and air–sea interaction in TOGA COARE and
719 DYNAMO, *J.*
720 *Climate*, 28(2), 597– 622. [https://doi.org/10.1175/JCLI-D-14-
721 00477.1](https://doi.org/10.1175/JCLI-D-14-00477.1), 2014.
- 722 de Szoek, S. P., Edson, J. B., Marion, J. R., Fairall, C. W., and Bariteau,

- 723 L.: The MJO and air–sea interaction in TOGA COARE and
724 DYNAMO, *J. Climate*, 28, 597–622, [https://doi.org/10.1175/JCLI-](https://doi.org/10.1175/JCLI-D-14-00477.1)
725 [D-14-00477.1](https://doi.org/10.1175/JCLI-D-14-00477.1), 2015.
- 726 de Szoeké, S. P., and Maloney, E.: Atmospheric mixed layer
727 convergence from observed MJO sea surface temperature
728 anomalies, *J. Climate*, 33(2), 547– 558. [https://doi.org/10.1175/JCLI-D-19-](https://doi.org/10.1175/JCLI-D-19-0351.1)
729 [0351.1](https://doi.org/10.1175/JCLI-D-19-0351.1), 2020.
- 731 Fu, J. X., Wang, W., Shinoda, T., Ren, H. L., and Jia, X.: Toward
732 understanding the diverse impacts of air–sea interactions on MJO
733 simulations, *J. Geophys. Res.- Oceans*, 122(11), 8855– 8875. [https://doi.org/10.1002/2017JC01318](https://doi.org/10.1002/2017JC013187)
734 [7](https://doi.org/10.1002/2017JC013187), 2017.
- 736 Gao, Y., Hsu, P.-C., Chen, L., Wang, L., and Li, T.: Effects of high-
737 frequency surface wind on the intraseasonal SST associated with the
738 Madden-Julian oscillation, *Clim. Dynam.*, 54, 4485–4498,
739 <https://doi.org/10.1007/s00382-020-05239-w>, 2020a.
- 740 Gao, Y., Klingaman, N. P., DeMott, C. A., and Hsu, P.-C.: Boreal
741 summer intraseasonal oscillation in a superparameterized general
742 circulation model: effects of air–sea coupling and ocean mean state,
743 *Geosci. Model Dev.*, 13, 5191–5209, [https://doi.org/10.5194/gmd-](https://doi.org/10.5194/gmd-13-5191-2020)
744 [13-5191-2020](https://doi.org/10.5194/gmd-13-5191-2020), 2020b.
- 745 Ge, X., Wang, W., Kumar, A., and Zhang, Y.: Importance of the vertical
746 resolution in simulating SST diurnal and intraseasonal variability in
747 an oceanic general circulation model, *J. Climate*, 30, 3963–
748 3978, <https://doi.org/10.1175/JCLI-D-16-0689.1>, 2017.
- 749 Gonzalez, A. O., and Jiang, X.: Winter mean lower tropospheric moisture
750 over the maritime continent as a climate model diagnostic metric for
751 the propagation of the Madden-Julian Oscillation, *Geophys. Res.*
752 *Lett.*, 44(5), 2588–2596. <https://doi.org/10.1002/2016GL072430>,
753 2017.
- 754 Hagos, S. M., Zhang, C., Feng, Z., Burleyson, C. D., Mott, C. De, Kerns,
755 B., Benedict, J. J., and Martini, M. N.: The impact of the diurnal
756 cycle on the propagation of Madden-Julian Oscillation convection
757 across the Maritime Continent, *J. Adv. Model. Earth Syst.*, 8, 1552–
758 1564, <https://doi.org/10.1002/2016MS000725>, 2016.
- 759 Hersbach, H., and Dee, D.: ERA5 reanalysis is in production, ECMWF
760 Newsletter, Vol. 147, p.
761 7, [https://www.ecmwf.int/en/newsletter/147/news/era5-reanalysis-](https://www.ecmwf.int/en/newsletter/147/news/era5-reanalysis-production)
762 [production](https://www.ecmwf.int/en/newsletter/147/news/era5-reanalysis-production), 2016.
- 763 Hong, X., Reynolds, C. A., Doyle, J. D., May, P., and O'Neill, L.:
764 Assessment of upper-ocean variability and the Madden-Julian
765 Oscillation in extended-range air–ocean coupled mesoscale
766 simulations, *Dyn. Atmos. Oceans*, 78, 89–105.

- 767 <https://doi.org/10.1016/j.dynatmoce.2017.03.002>, 2017.
- 768 Hsu, H.-H., and Lee, M.-Y.: Topographic effects on the eastward
769 propagation and initiation of the Madden-Julian Oscillation, *J.*
770 *Climate*, 18, 795-809, <https://doi.org/10.1175/JCLI-3292.1>, 2005.
- 771 Hurrell, J. W., Holland, M. M., Gent, P. R., Ghan, S., Kay, J. E., Kushner,
772 P. J., Lamarque, J.-F., Large, W. G., Lawrence, D., Lindsay, K.,
773 Lipscomb, W. H., Long, M. C., Mahowald, N., Marsh, D. R., Neale,
774 R. B., Rasch, P., Vavrus, S., Vertenstein, M., Bader, D., Collins, W.
775 D., Hack, J. J., Kiehl, J., and Marshall, S.: The Community Earth
776 System Model: A framework for collaborative research, *Bull. Amer.*
777 *Meteor. Soc.*, 94, 1339–1360, <https://doi.org/10.1175/BAMS-D-12-00121.1>, 2013.
- 779 Jiang, X., Waliser, D. E., Xavier, P. K., Petch, J., Klingaman, N. P.,
780 Woolnough, S. J., Guan, B., Bellon, G., Crueger, T., DeMott, C.,
781 Hannay, C., Lin, H., Hu, W., Kim, D., Lappen, C.-L., Lu, M.-M.,
782 Ma, H.-Y., Miyakawa, T., Ridout, J. A., Schubert, S. D., Scinocca,
783 J., Seo, K.-H., Shindo, E., Song, X., Stan, C., Tseng, W.-L., Wang,
784 W., Wu, T., Wu, X., Wyser, K., Zhang, G. J., and Zhu, H.: Vertical
785 structure and physical processes of the Madden-Julian oscillation:
786 Exploring key model physics in climate simulations, *J. Geophys.*
787 *Res.-Atmos.*, 120, 4718–4748,
788 <https://doi.org/10.1002/2014JD022375>, 2015.
- 789 Jiang, X.: Key processes for the eastward propagation of the Madden-
790 Julian Oscillation based on multimodel simulations, *J. Geophys. Res.*
791 *Atmos.*, 122, 755–770, <https://doi.org/10.1002/2016JD025955>, 2017.
- 792 Jiang, X., Adames, Á. F., Zhao, M., Waliser, D., and Maloney, E.: A
793 unified moisture mode framework for seasonality of the Madden-
794 Julian oscillation, *J. Climate*, 31, 4215–4224,
795 <https://doi.org/10.1175/JCLI-D-17-0671.1>, 2018.
- 796 Jiang, X., Adames, Á. F., Kim, D., Maloney, E. D., Lin, H., and Kim, H.,
797 Zhang, C., DeMott, C. A., and Klingaman, N. P.: Fifty years of
798 research on the Madden-Julian Oscillation: Recent progress,
799 challenges, and perspectives, *J. Geophys. Res.-Atmos.*, 125,
800 e2019JD030911, <https://doi.org/10.1029/2019JD030911>, 2020.
- 801 Kim, D., Kim, H., and Lee, M.-I.: Why does the MJO detour the Maritime
802 continent during Austral summer? *Geophys. Res. Lett.*, 44(5), 2579–
803 2587, <https://doi.org/10.1002/2017gl072643>, 2017.
- 804 Kim, H., Vitart, F., and Waliser, D. E.: Prediction of the Madden-Julian
805 oscillation: A review, *J. Climate*, 31(23), 9425–9443,
806 <https://doi.org/10.1175/JCLI-D-18-0210.1>, 2018.
- 807 Klingaman, N. P., and Demott, C. A.: Mean state biases and interannual
808 variability affect perceived sensitivities of the Madden-Julian
809 oscillation to air-sea coupling, *J. Adv. Model. Earth Syst.*, 12, 1–22,
810 <https://doi.org/10.1029/2019MS001799>, 2020.

- 811 Krishnamurti, T. N., Oosterhof, D. K. and Mehta, A. V.: Air–sea
812 interaction on the time scale of 30 to 50 days, *J. Atmos. Sci.*, 45,
813 1304–1322, [https://doi.org/10.1175/1520-0469\(1988\)045,1304:AIOTTS.2.0.CO;2](https://doi.org/10.1175/1520-0469(1988)045,1304:AIOTTS.2.0.CO;2), 1988.
- 815 Lambaerts, J., Lapeyre, G., Plougonven, R., and Klein, P.: Atmospheric
816 response to sea surface temperature mesoscale structures, *J.*
817 *Geophys. Res.-Atmos.*, 118(17), 9611–9621.
818 <https://doi.org/10.1002/jgrd.50769>, 2020.
- 819 Lan, Y.-Y., Hsu, H.-H., Tseng, W.-L., and Jiang, L.-C.: Embedding a
820 one-column ocean model in the Community Atmosphere Model 5.3
821 to improve Madden–Julian Oscillation simulation in boreal winter,
822 *Geosci. Model Dev.*, 15, 5689–5712, <https://doi.org/10.5194/gmd-15-5689-2022>, 2022.
- 824 Li, Y., Han, W., Shinoda, T., Wang, C., Ravichandran, M., and Wang,
825 J.-W.: Revisiting the wintertime intraseasonal SST variability in the
826 tropical south Indian Ocean: Impact of the ocean interannual
827 variation, *J. Phys. Oceanogr.*, 44, 1886–1907,
828 <https://doi.org/10.1175/JPO-D-13-0238.1>, 2014.
- 829 Li, T., Ling, J., and Hsu, P.-C.: Madden–Julian Oscillation: Its discovery,
830 dynamics, and impact on East Asia, *J. Meteor. Res.*, 34, 20–42,
831 <https://doi.org/10.1007/s13351-020-9153-3>, 2020a.
- 832 Li, K., Yu, W., Yang, Y., Feng, L., Liu, S., and Li, L.: Spring barrier to
833 the MJO eastward propagation, *Geophys. Res. Lett.*, 47, e2020GL087788, <https://doi.org/10.1029/2020GL087788>,
834 2020b.
- 836 Liang, Y.; Du, Y.; Zhang, L.; Zheng, X.; Qiu, S. The 30–50-Day
837 Intraseasonal Oscillation of SST and Precipitation in the South
838 Tropical Indian Ocean, *Atmos.*, 9, 69.
839 <https://doi.org/10.3390/atmos9020069>, 2018.
- 840 Liang, Y., and Du, Y.: Oceanic impacts on 50–80-day intraseasonal
841 oscillation in the eastern tropical Indian Ocean, *Clim. Dynam.*, 59,
842 1283–1296, <https://doi.org/10.1007/s00382-021-06041-y>, 2022.
- 843 Liebmann, B.: Description of a complete (interpolated) outgoing
844 longwave radiation dataset, *B. Am. Meteorol. Soc.*, 77, 1275–1277,
845 1996.
- 846 Madden, R. A., and Julian, P. R.: Description of global-scale circulation
847 cells in the tropics with a 40-50 day period, *J. Atmos. Sci.*, 29, 1109-
848 1123, [https://doi.org/10.1175/1520-0469\(1972\)029<1109:DOGSCC>2.0.CO;2](https://doi.org/10.1175/1520-0469(1972)029<1109:DOGSCC>2.0.CO;2), 1972.
- 850 Maloney, E., and Sobel, A. H.: Surface fluxes and ocean coupling in the
851 tropical intraseasonal oscillation. *J. Climate*, 17, 4368–4386,
852 <https://doi.org/10.1175/JCLI-3212.1>, 2004.
- 853 Newman, M., Sardeshmukh, P. D., and Penland, C.: How important is

- 854 air–sea coupling in ENSO and MJO evolution? *J.*
855 *Climate*, 22, 2958– 2977, <https://doi.org/10.1175/2008JCLI2659.1>,
856 2009.
- 857 Pariyar, S.K., Keenlyside, N., Tseng, W.-L., Hsu, H.-H., and Tsuang, B.-
858 J. The role of air–sea coupling on November–April intraseasonal
859 rainfall variability over the South Pacific, *Clim. Dynam.*, 60, 1121–
860 1136, <https://doi.org/10.1007/s00382-022-06354-6>, 2023.
- 861 Pei, S., Shinoda, T., Soloviev, A., and Lien, R.-C.: Upper ocean response
862 to the atmospheric cold pools associated with the Madden-Julian
863 Oscillation, *Geophys. Res. Lett.*, 45, 5020–5029,
864 <https://doi.org/10.1029/2018GL077825>, 2018.
- 865 Rasch, P. J., Xie, S., Ma, P.-L., Lin, W., Wang, H., Tang, Q., Bur-
866 rows, S. M., Caldwell, P., Zhang, K., Easter, R. C., Cameron-
867 Smith, P., Singh, B., Wan, H., Golaz, J.-C., Harrop, B. E., Roesler, E.,
868 Bacmeister, J., Larson, V. E., Evans, K. J., Qian, Y., Taylor, M.,
869 Leung, L. R., Zhang, Y., Brent, L., Branstet-
870 ter, M., Hannay, C., Mahajan, S., Mamatjanov, A., Neale, R., Richter, J. H., Yoon, J.-H.,
871 Zender, C. S., Bader, D., Flan-
872 ner, M., Foucar, J. G., Jacob, R.,
873 Keen, N., Klein, S. A., Liu, X., Salinger, A. G., Shrivastava, M., and
874 Yang, Y.: An overview of the atmospheric component of the Energy
875 Exascale Earth System Model, *J. Adv. Model Earth Sy.*, 11, 2377–
2411, <https://doi.org/10.1029/2019ms001629>, 2019.
- 876 Rayner, N. A., Parker, D. E., Horton, E. B., Folland, C. K., Alexander,
877 L. V., Rowell, D. P., Kent, E. C., and Kaplan, A.: Global analyses
878 of sea surface temperature, sea ice, and night marine air temperature
879 since the late nineteenth century, *J. Geophys. Res.*, 108(D14), 4407,
880 <https://doi.org/10.1029/2002JD002670>, 2003.
- 881 Ren, P. F., Gao, L., Ren, H.-L., Rong, X., and Li, J.: Representation of
882 the Madden–Julian Oscillation in CAMSCSM, *J. Meteor. Res.*, 33,
883 627–650, <https://doi.org/10.1007/s13351-019-8118-x>, 2019.
- 884 Savarin, A., and Chen, S. S.: Pathways to better prediction of the MJO:
885 2. Impacts of atmosphere-ocean coupling on the upper ocean and
886 MJO propagation, *J. Adv. Model. Earth Syst.*, 14, e2021MS002929,
887 <https://doi.org/10.1029/2021MS002929>, 2022.
- 888 Shinoda, T., Pei, S., Wang, W., Fu, J. X., Lien, R.-C., Seo, H.,
889 and Soloviev, A.: Climate process team: Improvement of ocean
890 component of NOAA climate forecast system relevant to Madden-
891 Julian Oscillation simulations, *J. Adv. Model. Earth Syst.*, 13(12),
892 e2021MS002658. <https://doi.org/10.1029/2021MS002658>, 2021.
- 893 Seo, H., Subramanian, A. C., Miller, A. J., and Cavanaugh, N.
894 R.: Coupled impacts of the diurnal cycle of sea surface temperature
895 on the Madden–Julian
896 oscillation, *J. Climate*, 27(22), 8422– 8443. <https://doi.org/10.1175/JCLI-D-14-00141.1>, 2014.

- 898 Sobel, A. H., and Gildor, H.: A simple time-dependent model of SST hot
899 spots. *J. Climate*, 16, 3978–3992, [https://doi.org/10.1175/1520-0442\(2003\)016<3978:ASTMOS>2.0.CO;2](https://doi.org/10.1175/1520-0442(2003)016<3978:ASTMOS>2.0.CO;2), 2003.
- 901 Sobel, A. H., Maloney, E. D., Bellon, G., and Frierson, D. M.: Surface
902 Fluxes and Tropical Intraseasonal Variability: a Reassessment, *J.*
903 *Adv. Model. Earth Syst.*, 2, 2, 2,
904 <https://doi.org/10.3894/JAMES.2010.2.2>, 2010.
- 905 Sobel, A., Wang, S., and Kim, D.: Moist static energy budget of the MJO
906 during DYNAMO, *J. Atmos. Sci.*, 71(11), 4276– 4291,
907 <https://doi.org/10.1175/JAS-D-14-0052.1>, 2014.
- 908 Stan, C.: The role of SST variability in the simulation of the MJO, *Clim.*
909 *Dynam.*, 51, 2943–2964, <https://doi.org/10.1007/s00382-017-4058-2>, 2018.
- 911 Tseng, W.-L., Tsuang, B.-J., Keenlyside, N. S., Hsu, H.-H. and Tu, C.-
912 Y.: Resolving the upper-ocean warm layer improves the simulation
913 of the Madden-Julian oscillation, *Clim. Dynam.*, 44, 1487–1503,
914 <https://doi.org/10.1007/s00382-014-2315-1>, 2015.
- 915 Tseng, W.-L., Hsu, H.-H., Keenlyside, N., Chang, C.-W. J., Tsuang, B.-
916 J., Tu, C.-Y., and Jiang, L.-C.: Effects of Orography and Land–Sea
917 Contrast on the Madden–Julian Oscillation in the Maritime
918 Continent: A Numerical Study Using ECHAM-SIT, *J. Climate*, 30,
919 9725–9741, <https://doi.org/10.1175/JCLI-D-17-0051.1>, 2017.
- 920 Tseng, W.-L., Hsu, H.-H., Lan, Y.-Y., Lee, W.-L., Tu, C.-Y., Kuo, P.-
921 H., Tsuang, B.-J., and Liang, H.-C.: Improving Madden–Julian
922 oscillation simulation in atmospheric general circulation models by
923 coupling with a one-dimensional snow–ice–thermocline ocean
924 model, *Geosci. Model Dev.*, 15, 5529–5546,
925 <https://doi.org/10.5194/gmd-15-5529-2022>, 2022.
- 926 Tulich, S. N., and Kiladis, G. N.: On the Regionality of moist kelvin
927 waves and the MJO: The critical role of the background zonal flow,
928 *J. Adv. Model. Earth Syst.*, 13(9), e2021MS002528.
929 <https://doi.org/10.1029/2021MS002528>, 2021.
- 930 Voldoire, A., Roehrig, R., Giordani, H., Waldman, R., Zhang, Y., Xie,
931 S., and Bouin, M.-N.: Assessment of the sea surface temperature
932 diurnal cycle in CNRM-CM6-1 based on its 1D coupled
933 configuration, *Geosci. Model Dev.*, 15, 3347–3370,
934 <https://doi.org/10.5194/gmd-15-3347-2022>, 2022.
- 935 Wang, W., Hung, M.-P., Weaver, S. J., Kumar, A., and Fu, X.: MJO
936 prediction in the NCEP Climate Forecast System version 2, *Clim.*
937 *Dynam.*, 42, 2509–2520, <https://doi.org/10.1007/s00382-013-1806-9>, 2014.
- 939 Wang, L. and Li, T.: Effect of vertical moist static energy advection on
940 MJO eastward propagation: Sensitivity to analysis domain, *Clim.*
941 *Dynam.*, 54, 2029–2039, <https://doi.org/10.1007/s00382-019-31>

- 942 05101-8, 2020.
- 943 Watterson, I. G.: The sensitivity of subannual and intraseasonal tropical
944 variability to model ocean mixed layer depth, *J. Geophys. Res.*, 107,
945 4020, <https://doi.org/10.1029/2001JD000671>, 2002.
- 946 Wheeler, M. C., and Hendon, H. H.: An all-season real-time multivariate
947 MJO index: development of an index for monitoring and prediction,
948 *Mon. Weather Rev.*, 132, 1917–1932, [https://doi.org/10.1175/1520-0493\(2004\)132<1917:AARMMI>2.0.CO;2](https://doi.org/10.1175/1520-0493(2004)132<1917:AARMMI>2.0.CO;2), 2004.
- 950 Wheeler, M., and Kiladis, G. N.: Convectively coupled equatorial waves:
951 Analysis of clouds and temperature in the wavenumber-frequency
952 domain, *J. Atmos. Sci.*, 56, 374–399, [https://doi.org/10.1175/1520-0469\(1999\)056<0374:CCEWAO>2.0.CO;2](https://doi.org/10.1175/1520-0469(1999)056<0374:CCEWAO>2.0.CO;2), 1999.
- 954 Wu, C.-H., and Hsu, H.-H.: Potential Influence of Topography on the
955 MJO in the Maritime Continent, *J. Climate*, 22, 5433-5448,
956 <https://doi.org/10.1175/2009JCLI2825.1>, 1999.
- 957 Wu, J., Li, Y., Luo, J.-J. and Jiang, X.: Assessing the role of air–sea
958 coupling in predicting Madden–Julian oscillation with an
959 Atmosphere–Ocean coupled model, *J. Clim.* 34 9647–63,
960 <https://doi.org/10.1175/JCLI-D-20-0989.1>, 2021.
- 961 Zhang, L., and Han, W.: Barrier for the eastward propagation of
962 Madden–Julian Oscillation over the maritime continent: A possible
963 new mechanism, *Geophys. Res. Lett.*, 47(21),
964 e2020GL090211. <https://doi.org/10.1029/2020gl090211>, 2020.
- 965 Zhao, N., and Nasuno, T.: How Does the Air–Sea Coupling Frequency
966 Affect Convection During the MJO Passage?, *J. Adv. Model. Earth
967 Sy.*, 12, e2020MS002058, <https://doi.org/10.1029/2020MS002058>,
968 2020.

969 Table 1. Two sets of experiments with different SST feedback
 970 frequencies: high-frequency (C-CTL, C-1day and C-3days) and low-
 971 frequency (C-6days, C-12days, C-18days, C-24days and C-30days).

972

subseasonal sets	high-frequency SST (< 6 days)			low-frequency SST (6-30 days)				
experiments	C-CTL	C-1day	C-3days	C-6days	C-12days	C-18days	C-24days	C-30days
atmosphere to ocean frequency	48/1day							
ocean to atmosphere Frequency	48/1day	1/1day	1/3days	1/6days	1/12days	1/18days	1/24days	1/30days

973

974 Table 2. Key intraseasonal (20–100-day bandpass filtered) ocean temperatures in all
 975 experiments: SST, differences between SST and temperatures at 10m depth ($\overline{\Delta T_{0-10m}}$)
 976 and 30m depth ($\overline{\Delta T_{0-30m}}$), t max/mini SST and 10m-depth temperature (T_{10m}) in the
 977 area of (110–130° E, 5–15° S) during a MJO cycle for the observation (OISST), AGCM
 978 (A–CTL), high-frequency experiments (C–CTL, C–1day, and C–3days), and low-
 979 frequency experiments (C–6days, C–12days, C–18days, C–24days, and C–30days)
 980

(110–130° E, 5–15° S)		obs.	AGC M	high-frequency			low-frequency				
experiments		OI SST ¹	A– CTL ²	C– CTL	C– 1day	C– 3days	C– 6days	C– 12days	C– 18days	C– 24days	C– 30days
DJF seasonal mean	SST	302.2 ±0.96	302.2 ±0.77	300.8 ±0.76	301.2 ±0.76	301.2 ±0.75	301.2 ±0.75	301.4 ±0.75	301.6 ±0.80	302.0 ±1.06	302.7 ±1.71
	$\overline{\Delta T_{0-10m}}$	-	-	0.1 ± 0.22	0.1 ± 0.22	0.1 ± 0.21	0.1 ± 0.23	0.2 ± 0.25	0.3 ± 0.32	0.5 ± 0.50	1.0 ± 0.95
	$\overline{\Delta T_{0-30m}}$	-	-	0.8 ± 0.79	0.7 ± 0.70	0.6 ± 0.69	0.8 ± 0.70	0.8 ± 0.70	1.0 ± 0.73	1.4 ± 0.96	2.1 ± 1.54
phase's mean in boreal winter	max (phase) SST	0.21 (ph2)	0.02 (ph2)	0.24 (ph3)	0.26 (ph3)	0.22 (ph3)	0.32 (ph3)	0.36 (ph3)	0.43 (ph3)	0.50 (ph3)	0.62 (ph2)
	max T_{10m} (phase)	-	-	0.15 (ph4)	0.17 (ph4)	0.14 (ph3)	0.19 (ph3)	0.21 (ph3)	0.26 (ph3)	0.30 (ph3)	0.35 (ph2)
	mini (phase) SST	-0.21 (ph7)	-0.003 (ph8)	-0.17 (ph7)	-0.22 (ph7)	-0.19 (ph7)	-0.25 (ph7)	-0.28 (ph7)	-0.38 (ph7)	-0.52 (ph6)	-0.60 (ph6)
	mini T_{10m} (phase)	-	-	-0.11 (ph8)	-0.12 (ph7)	-0.11 (ph8)	-0.15 (ph7)	-0.17 (ph7)	-0.24 (ph7)	-0.33 (ph6)	-0.33 (ph6)

981 Note: ¹daily average data, ² monthly average data.

格式化表格

982 **Figure List**

983 **Figure 1.** Wavenumber–frequency spectra for 850-hPa zonal wind averaged over 10°
984 S – 10° N in boreal winter after removing the climatological mean seasonal cycle.
985 Vertical dashed lines represent periods at 80 and 30 days. (a)–(j) are from ERA5
986 reanalysis, A–CTL, C–CTL, C–1day, C–3days, C–6days, C–12days, C–18days, C–
987 24days, and C–30days, respectively.

988
989 **Figure 2.** Hovmöller diagrams of correlation between precipitation averaged over 10°
990 S – 5° N , 75 – 100° E and precipitation (color) and 850-hPa zonal wind (contour)
991 averaged over 10° N – 10° S . (a)–(j) are arranged in the same order as in Fig. 1 for
992 GPCP/ERA5 and all experiments. All data are 20–100-day bandpass filtered.

993
994 **Figure 3.** Zonal wavenumber–frequency power spectra of anomalous OLR (colors) and
995 phase lag with U850 (vectors) for the symmetric component of tropical waves, with the
996 vertically upward vector representing a phase lag of 0° and phase lag increasing
997 clockwise. Three dispersion straight lines with increasing slopes representing the
998 equatorial Kelvin waves (derived from the shallow water equations) corresponding to
999 three equivalent depths, 12, 25, and 50 m, respectively. (a)–(j) are arranged in the same
1000 order as in Fig. 1 for NOAA/ERA5 and all experiments.

1001
1002 **Figure 4.** Phase-longitude Hovmöller diagrams of 20–100-day filtered precipitation
1003 (mm day^{-1} , shaded) and SST anomaly (K, contour) averaged over 10° N – 10° S from
1004 phase 1 to 8. Contour interval is 0.03; solid, dashed, and thick-black lines represent
1005 positive, negative, and zero values, respectively. (a)–(j) are arranged in the same order
1006 as in Fig. 1 for NOAA/ERA5 and all experiments.

1007
1008 **Figure 5.** Phase-vertical Hovmöller diagrams of 20–100-day specific humidity
1009 (g kg^{-1} , shading) and air temperature (contoured, K) averaged over 5 – 20° S , 120 – 150°
1010 E ; solid, dashed, and thick-black curves are positive, negative, and zero values,
1011 respectively. (a)–(j) are arranged in the same order as in Fig. 1 for NOAA/ERA5 and
1012 all experiments.

1013
1014 **Figure 6.** The 20–100-day filtered oceanic temperature (K, shaded and contour,
1015 interval 0.03) at phase 2–3 (Left column) and phase 4–5 (Right column) averaged
1016 over 0 – 15° S between 0 and 60 m depth. (a)–(b) are from C–CTL, (c)–(d) are from
1017 C–1day, (e)–(f) are from C–3days, (g)–(h) are from C–6days, (i)–(j) are from C–
1018 12days, (k)–(l) are from C–18days, (m)–(n) are from C–24days, and (o)–(p) are from
1019 C–30days.

1020

1021 **Figure 7.** The lead-lag relationship between MJO-related atmosphere and SST
1022 variation from phase 1 to 8 averaged within 110–130° E and 5–15° S. The variables
1023 analyzed include 20-100-day filtered LHF, green shading), OLR (yellow bar chart),
1024 FSNS, (orange bar chart), U850 (purple bar chart), 30-m T (multiplied by 100, black
1025 line), and SST (multiplied by 10, orange line). Variables denoted with L (R) are scaled
1026 by the left (right) y-axis. (a)–(j) are from ERA5/OISST reanalysis, A-CTL, C-CTL, C-
1027 1day, C-3days, C-6days, C-12days, C-18days, C-24days, and C-30days, respectively.
1028

1029 **Figure 8.** Averaged 20–100-day filtered fields at phase 2–3. (Upper row) OLR (W m^{-2} ,
1030 shaded) and 200 hPa zonal and meridional wind anomaly (m s^{-1} , vector with reference
1031 vector shown at the top right corner, latent heat flux (W m^{-2} , shaded, positive
1032 representing upward), and 10-m wind anomaly (m s^{-1} , contour interval 0.5). (Second
1033 row) net surface heat flux (W m^{-2} , shaded) and net solar radiation (W m^{-2} , contour
1034 interval 6). (Third row) SST (K, shaded) and 850 hPa zonal and meridional wind
1035 anomaly (m s^{-1} , vector with reference vector shown at the top right corner. The number
1036 of days used to generate the composite is shown at the bottom right corner. (a), (d), (g)
1037 and (j) are from C-18days; (b), (e), (h) and (k) are from C-24days, and (c), (f), (i) and
1038 (l) are from C-30days, respectively. Solid, dashed, and thick-black lines represent
1039 positive, negative, and zero values, respectively.
1040

1041 **Figure 9.** Averaged 20–100-day filtered column-integrated MSE budget terms
1042 ($\text{J kg}^{-1} \text{ s}^{-1}$) in 10° S–0° N/S, 120–150° E for ERA5 and all model simulations. Colors
1043 represent different datasets: green for REA5, light blue for A-CTL, red, orange and
1044 navy blue for high-frequency experiments (C-CTL, C-1day, and C-3days,
1045 respectively), purple, black, dark brown, dark green, and dark gray for low-frequency
1046 experiments (C-6days, C-12days, C-18days, C-24days, and C-30days, respectively).
1047 The bars from left to right represent MSE tendency ($\langle \text{dmdt} \rangle$), vertical MSE advection
1048 ($\langle \text{wdmdp} \rangle$), horizontal MSE advection ($\langle \text{vdm} \rangle$), surface latent heat flux (LH),
1049 surface sensible heat flux (SH), shortwave radiation flux ($\langle \text{SW} \rangle$), longwave radiation
1050 flux ($\langle \text{LW} \rangle$), and residual terms.
1051

1052 **Figure 10.** Filtered the column-integrated MSE tendency ($\text{J kg}^{-1} \text{ s}^{-1}$, shading),
1053 precipitation (mm d^{-1} , contours interval 1.5) and 850-hPa wind (green vector, reference
1054 vector 2 m s^{-1}) in phase 5: (a) ERA5, (b) A-CTL, (c) C-CTL, (d) C-1day, (e) C-3days,
1055 (f) C-6days, (g) C-12days, (h) C-18days, (i) C-24days, and (i) C-30days. Solid-red,
1056 dashed-blue, and thick-black curves represent positive, negative, and zero values,
1057 respectively.

已删除: gray

已删除: wathet

1060

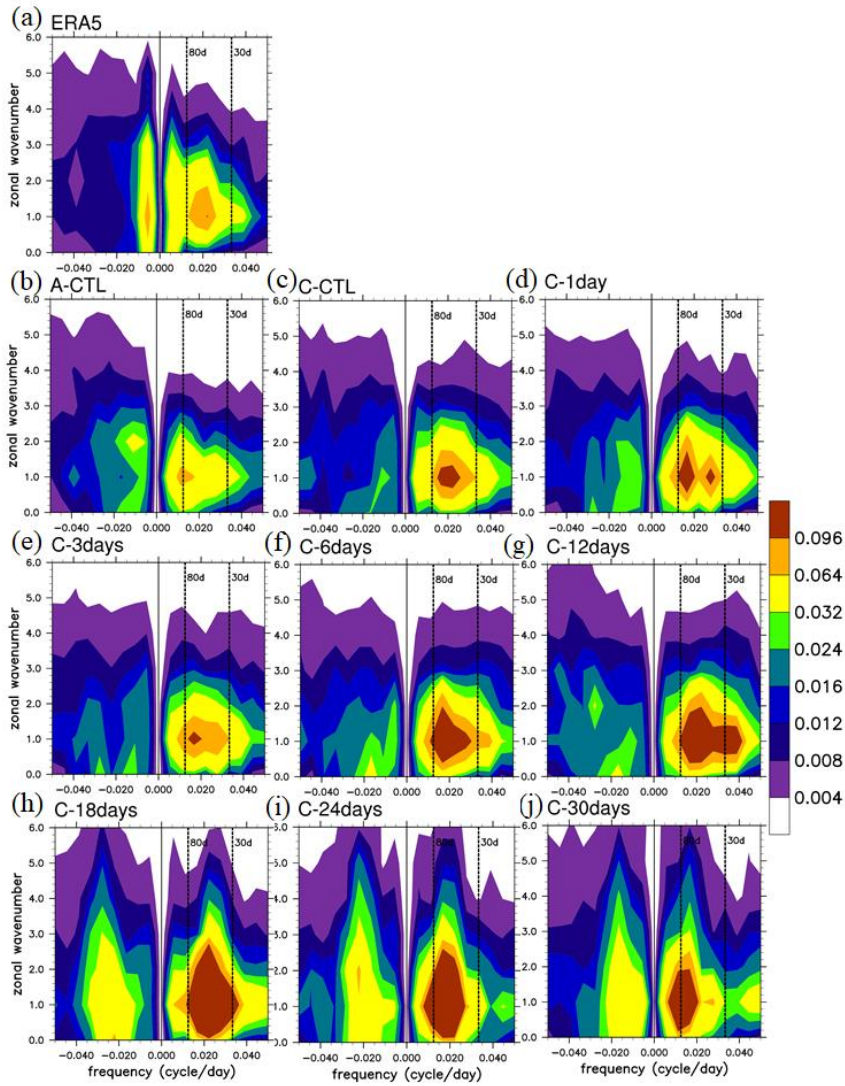
1061 **Figure 11.** The projection of each MSE component onto the ERA5 column-integrated
1062 MSE tendency at phase 5 over the MC (20° S–20° N, 90–210° E): $\langle \text{dmdt} \rangle$, $\langle \text{wdmdp} \rangle$,
1063 $\langle \text{vdm} \rangle$, Q_r , F_s , and residual; decomposition of horizontal MSE advection to zonal and
1064 meridional advection ($\langle \text{udmdt} \rangle$ and $\langle \text{vmdy} \rangle$).

1065

1066 **Figure 12.** Filtered column-integrated vertical ($\text{J kg}^{-1} \text{ s}^{-1}$, shading) and horizontal MSE
1067 advection ($\text{J kg}^{-1} \text{ s}^{-1}$, contours interval 6.0), and 200-hPa wind (green vector with
1068 reference vector 3 m s^{-1}): (a) ERA5, (b) A-CTL, (c) C-CTL, (d) C-1day, (e) C-3days,
1069 (f) C-6days, (g) C-12days, (h) C-18days, (i) C-24days, and (j) C-30days. Solid-blue,
1070 dashed-red, and thick-black curves represent positive, negative, and zero values,
1071 respectively.

1072

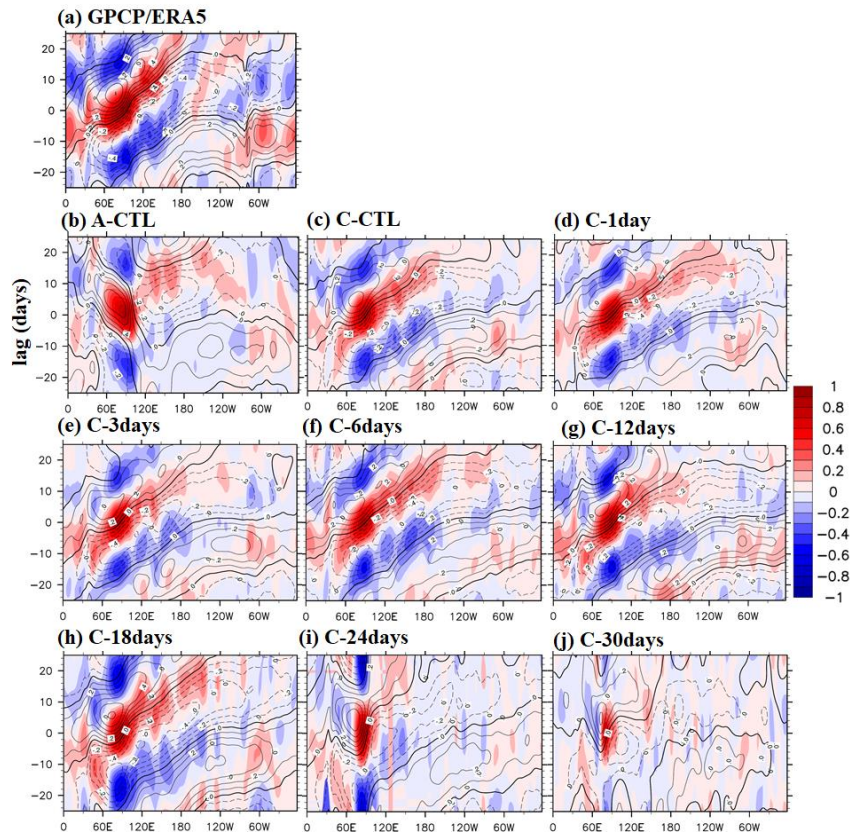
1073 **Figure 13.** Schematic diagrams illustrate the anomalous circulation and moistening
1074 processes during the eastward propagation of the MJO in experiments: (a) A-CTL, (b)
1075 high-frequency SST feedback experiments (C-CTL, C-1day, and C-3days), (c) low-
1076 frequency SST feedback experiments (C-6days, C-12days, and C-18days), and (d)
1077 C-24days and C-30days experiment. In each panel, the horizontal line represents the
1078 equator. The size of clustering gray clouds indicates the strength of convective
1079 organization. A red ellipse indicates convection-driven circulation. In the coupled
1080 simulations, light red (blue) filled ovals represent warm (cold) SST anomalies,
1081 respectively, and grass green filled rectangle represent latent heat flux. Unresolved
1082 convective processes are indicated by black dots representing low-level moisture
1083 convergence. Low-level moisture convergence into the equatorial trough is shown by
1084 light blue arrows, while midlevel moisture advection is represented by left-pointing
1085 green arrows. The deeper colors or thicker lines on the map indicate stronger anomalies
1086 of the MJO perturbations. Note: The concept of the figure is based on DeMott et al.
1087 (2014).



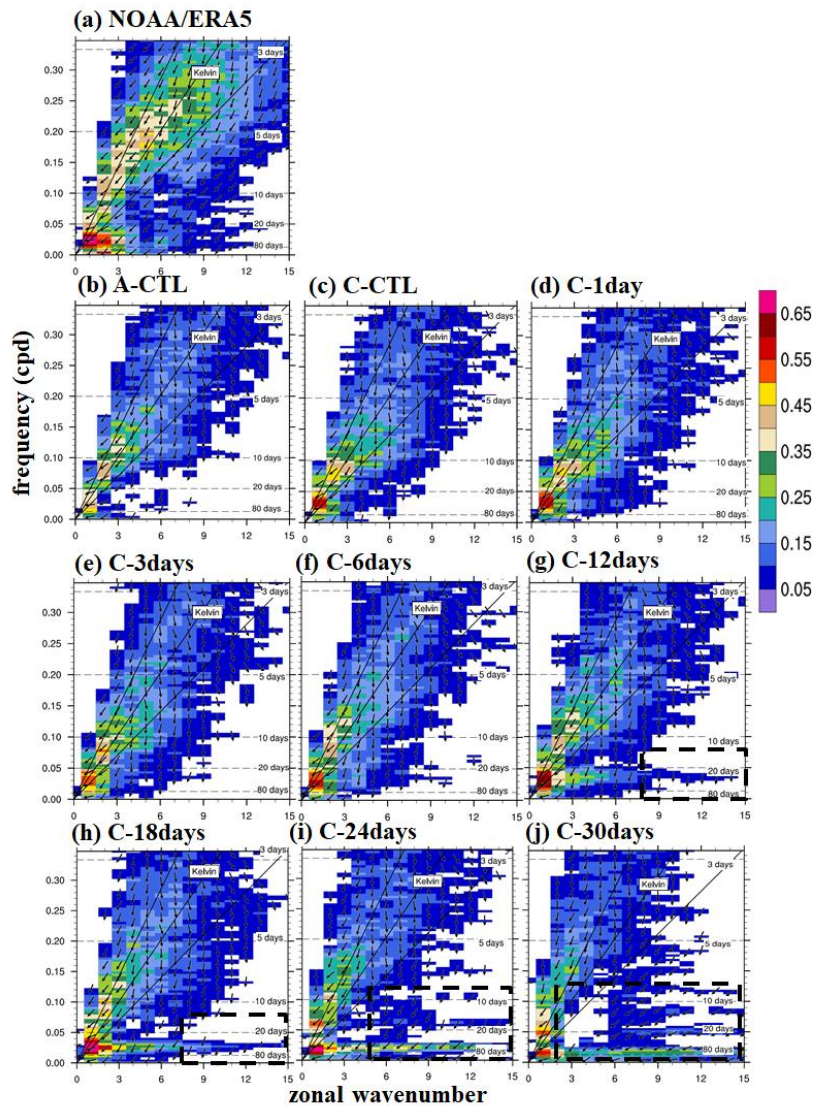
1088

1089 **Figure 1.** Wavenumber–frequency spectra for 850-hPa zonal wind averaged over 10°
 1090 S–10° N in boreal winter after removing the climatological mean seasonal cycle.
 1091 Vertical dashed lines represent periods at 80 and 30 days. (a)–(j) are from ERA5
 1092 reanalysis, A–CTL, C–CTL, C–1day, C–3days, C–6days, C–12days, C–18days, C–
 1093 24days, and C–30days, respectively.

1094

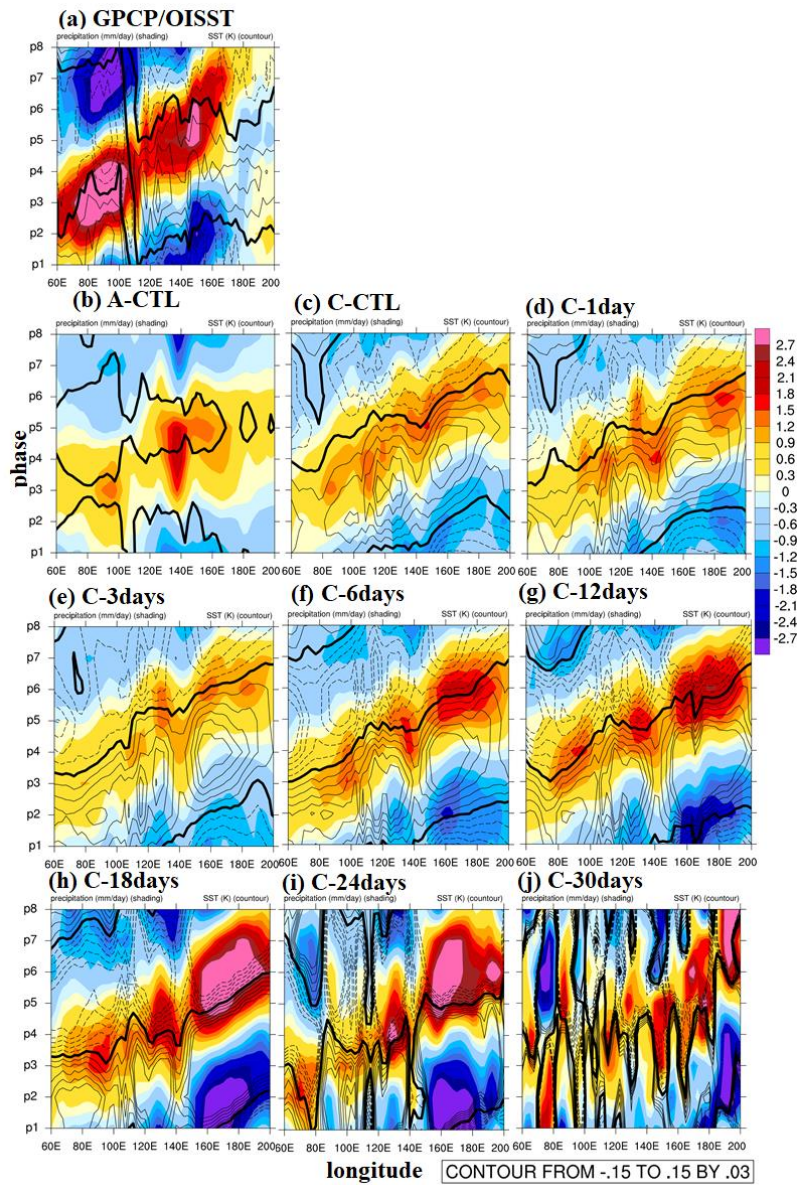


1095
 1096 **Figure 2.** Hovmöller diagrams of correlation between precipitation averaged over 10°
 1097 $S-5^{\circ} N$, $75-100^{\circ} E$ and precipitation (color) and 850-hPa zonal wind (contour)
 1098 averaged over $10^{\circ} N-10^{\circ} S$. (a)–(j) are arranged in the same order as in Fig. 1 for
 1099 GPCP/ERA5 and all experiments. All data are 20–100-day bandpass filtered.
 1100



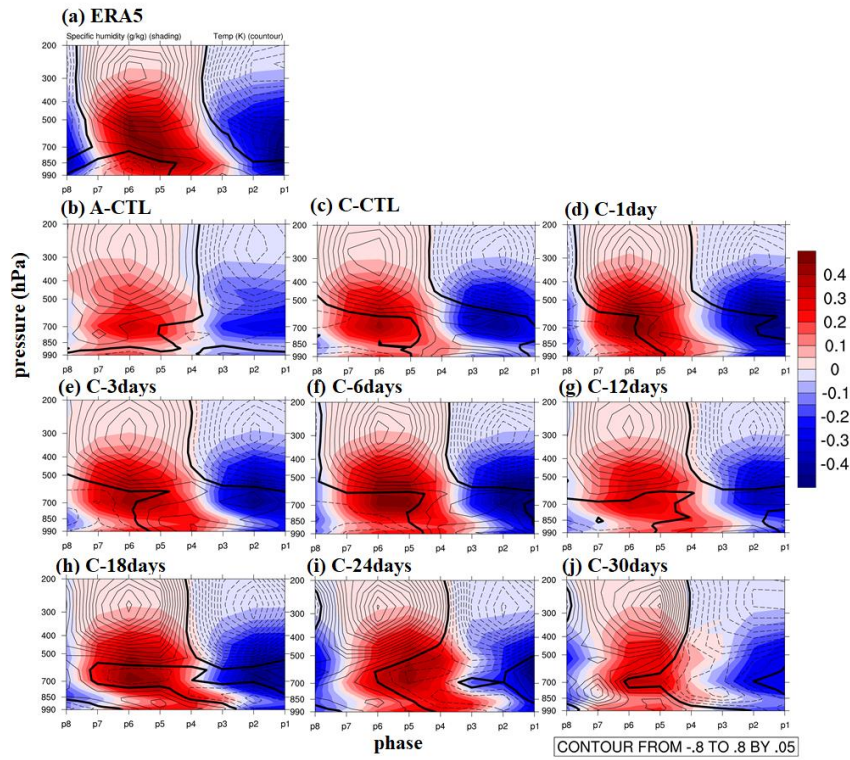
1101

1102 **Figure 3.** Zonal wavenumber–frequency power spectra of anomalous OLR (colors) and
 1103 phase lag with U850 (vectors) for the symmetric component of tropical waves, with the
 1104 vertically upward vector representing a phase lag of 0° with phase lag increasing
 1105 clockwise. Three dispersion straight lines with increasing slopes represent the
 1106 equatorial Kelvin waves (derived from the shallow water equations) corresponding to
 1107 three equivalent depths, 12, 25, and 50 m, respectively. (a)–(j) arrange in order are same
 1108 order as in Fig. 1 for NOAA/ERA5 and all experiments.

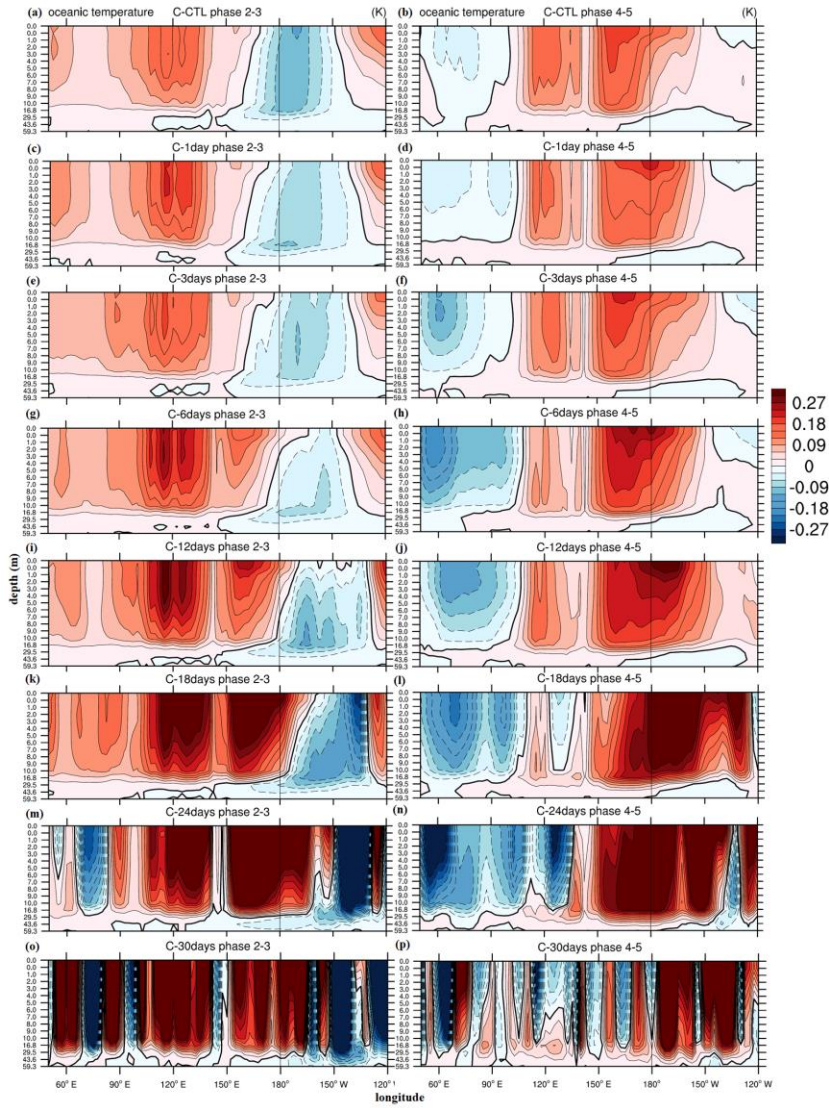


1109

1110 **Figure 4.** Phase-longitude Hovmöller diagrams of 20–100-day filtered precipitation
 1111 (mm day⁻¹, shaded) and SST anomaly (K, contour) averaged over 10° N–10° S from
 1112 phase 1 to 8. Contour interval is 0.03; solid, dashed, and thick-black lines represent
 1113 positive, negative, and zero values, respectively. (a)–(j) are arranged in the same order
 1114 as in Fig. 1 for NOAA/ERA5 and all experiments.

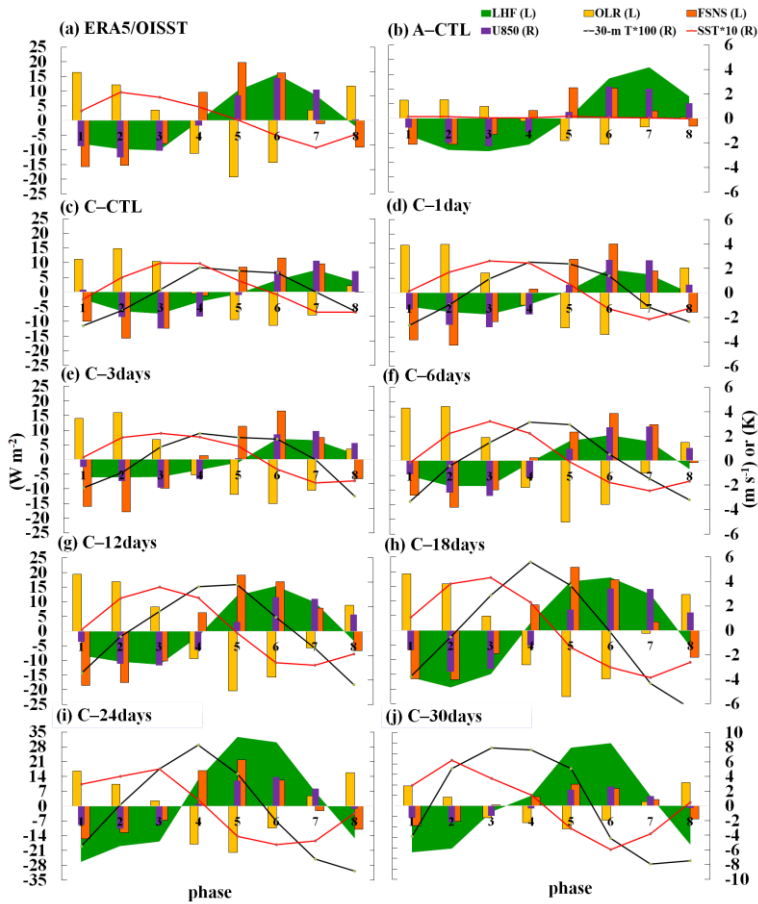


1116
 1117 **Figure 5.** Phase-vertical Hovmöller diagrams of 20–100-day specific humidity
 1118 (shading, g kg^{-1}) and air temperature (contoured, K) averaged over $5\text{--}20^\circ\text{S}$, $120\text{--}150^\circ$
 1119 E; solid, dashed, and thick-black curves are positive, negative, and zero values,
 1120 respectively. (a)–(j) are arranged in the same order as in Fig. 1 for NOAA/ERA5 and
 1121 all experiments.
 1122



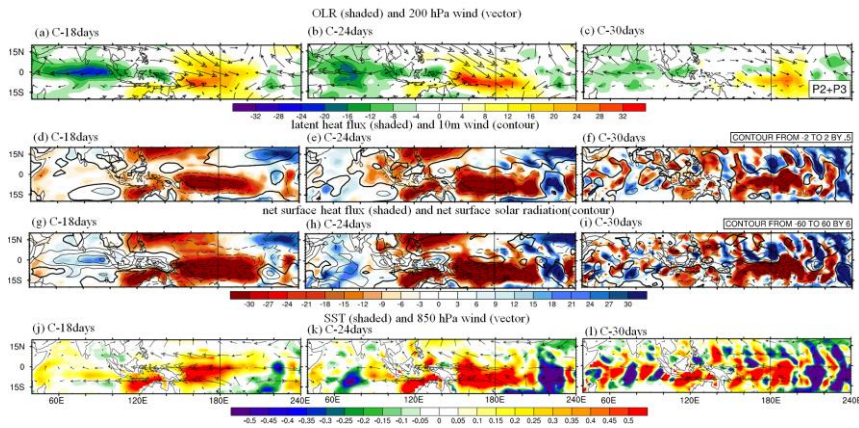
1124

1125 **Figure 6.** The 20–100-day filtered oceanic temperature (K, shaded and contour, interval
 1126 0.03) at phase 2–3 (Left column) and phase 4–5 (Right column) averaged over 0–15°
 1127 S between 0 and 60 m depth. (a)–(b) are from C–CTL, (c)–(d) are from C–1day, (e)–(f)
 1128 are from C–3days, (g)–(h) are from C–6days, (i)–(j) are from C–12days, (k)–(l) are
 1129 from C–18days, (m)–(n) are from C–24days, and (o)–(p) are from C–30days.



1130

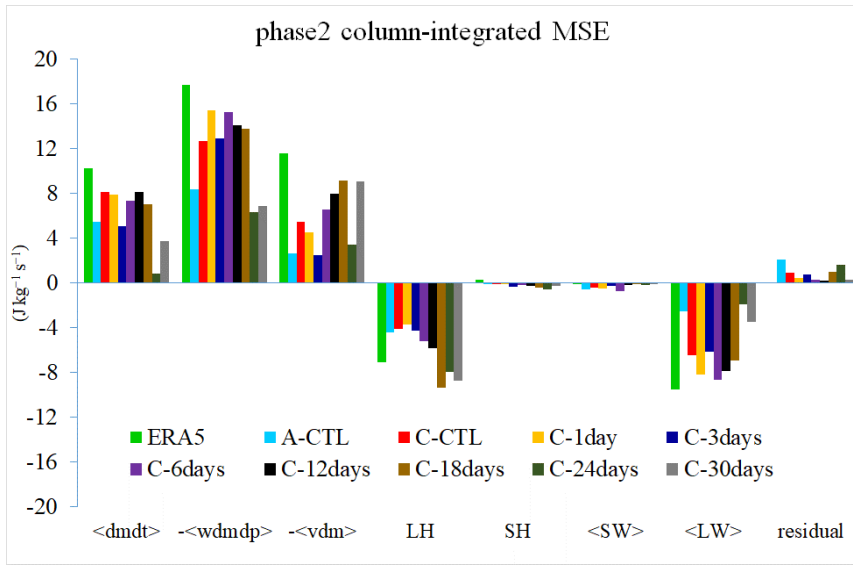
1131 **Figure 7.** The lead-lag relationship between MJO-related atmosphere and SST
 1132 variation from phase 1 to 8 averaged within 110–130° E and 5–15° S. The variables
 1133 analyzed include 20-100-day filtered LHF, green shading), OLR (yellow bar chart),
 1134 FSNS, (orange bar chart), U850 (purple bar chart), 30-m T (multiplied by 100, black
 1135 line), and SST (multiplied by 10, orange line). Variables denoted with L (R) are scaled
 1136 by the left (right) y-axis. (a)–(j) are from ERA5/OISST reanalysis, A-CTL, C-CTL, C-
 1137 1day, C-3days, C-6days, C-12days, C-18days, C-24days, and C-30days, respectively.



1138

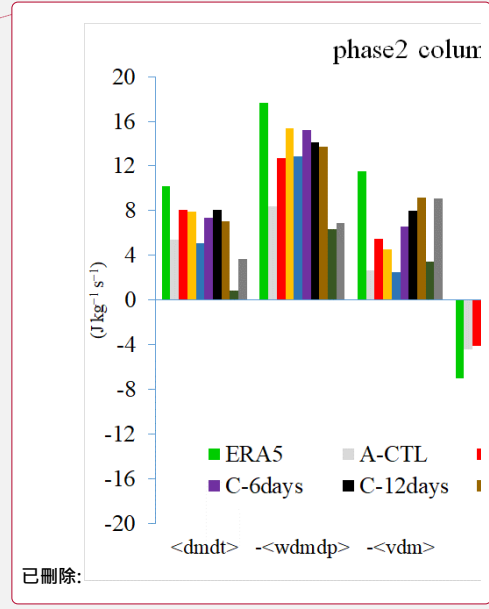
1139 **Figure 8.** Averaged 20–100-day filtered fields at phase 2–3. (Upper row) OLR (W m^{-2} ,
 1140 shaded) and 200 hPa zonal and meridional wind anomaly (m s^{-1} , vector with reference
 1141 vector shown at the top right corner, latent heat flux (W m^{-2} , shaded, positive
 1142 representing upward), and 10-m wind anomaly (m s^{-1} , contour interval 0.5). (Second
 1143 row) net surface heat flux (W m^{-2} , shaded) and net solar radiation (W m^{-2} , contour
 1144 interval 6). (Third row) SST (K , shaded) and 850 hPa zonal and meridional wind
 1145 anomaly (m s^{-1} , vector with reference vector shown at the top right corner. The number
 1146 of days used to generate the composite is shown at the bottom right corner. (a), (d), (g)
 1147 and (j) are from C–18days; (b), (e), (h) and (k) are from C–24days, and (c), (f), (i) and
 1148 (l) are from C–30days, respectively. Solid, dashed, and thick-black lines represent
 1149 positive, negative, and zero values, respectively.

1150



1151

1152 **Figure 9.** Averaged 20–100-day filtered column-integrated MSE budget terms
 1153 ($\text{J kg}^{-1} \text{ s}^{-1}$) in $10^\circ \text{ S} - 0^\circ \text{ N/S}$, $120 - 150^\circ \text{ E}$ for ERA5 and all model simulations.
 1154 Colors represent different datasets: green for ERA5, light blue for A-CTL, red, orange
 1155 and navy blue for high-frequency experiments (C-CTL, C-1day, and C-3days,
 1156 respectively), purple, black, dark brown, dark green, and dark gray for low-frequency
 1157 experiments (C-6days, C-12days, C-18days, C-24days, and C-30days, respectively).
 1158 The bars from left to right represent MSE tendency ($\langle \text{dmdt} \rangle$), vertical MSE advection
 1159 ($-\langle \text{wdmdp} \rangle$), horizontal MSE advection ($-\langle \text{vdm} \rangle$), surface latent heat flux (LH),
 1160 surface sensible heat flux (SH), shortwave radiation flux ($\langle \text{SW} \rangle$), longwave radiation
 1161 flux ($\langle \text{LW} \rangle$), and residual terms.

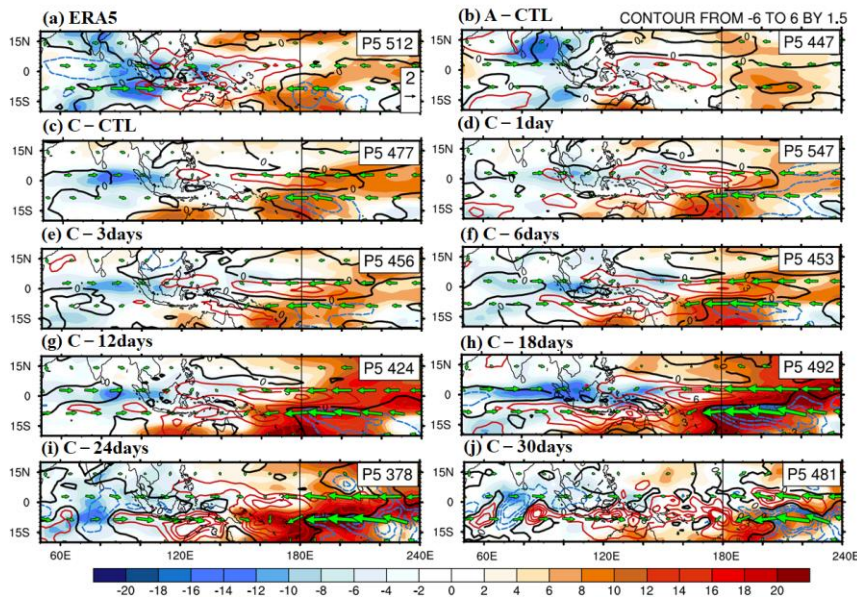


已删除:

已删除: gray

已删除: wathet

1165

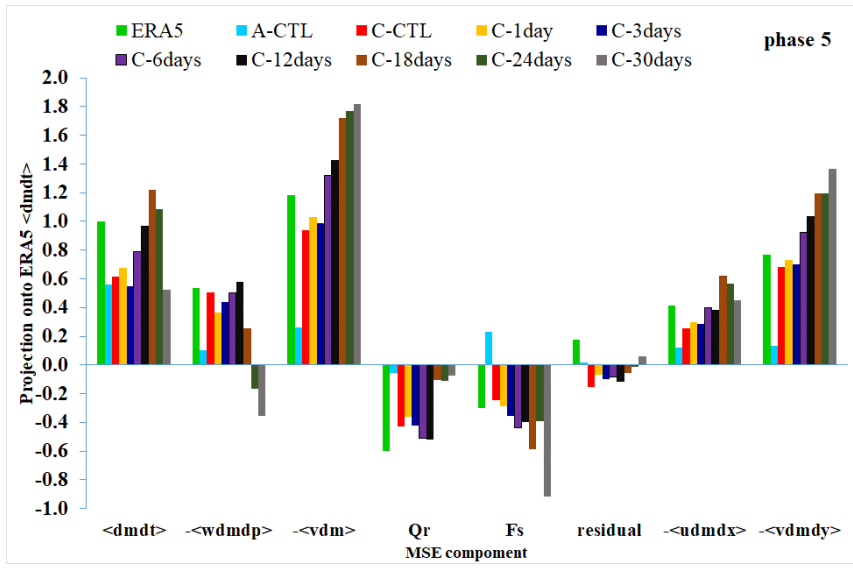


1166

1167 **Figure 10.** Filtered the column-integrated MSE tendency ($\text{J kg}^{-1} \text{s}^{-1}$, shading),
1168 precipitation (mm d^{-1} , contours interval 1.5) and 850-hPa wind (green vector,
1169 reference vector 2 m s^{-1}) in phase 5: (a) ERA5, (b) A-CTL, (c) C-CTL, (d) C-1day,
1170 (e) C-3days, (f) C-6days, (g) C-12days, (h) C-18days, (i) C-24days, and (j)
1171 C-30days. Solid-red, dashed-blue, and thick-black curves represent positive, negative,
1172 and zero values, respectively.

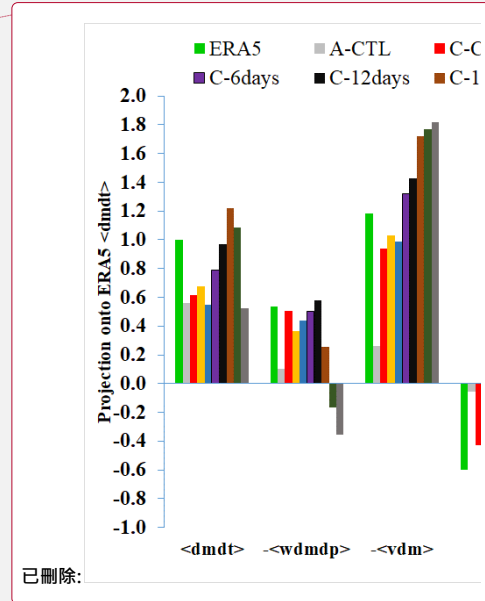
1173

1174

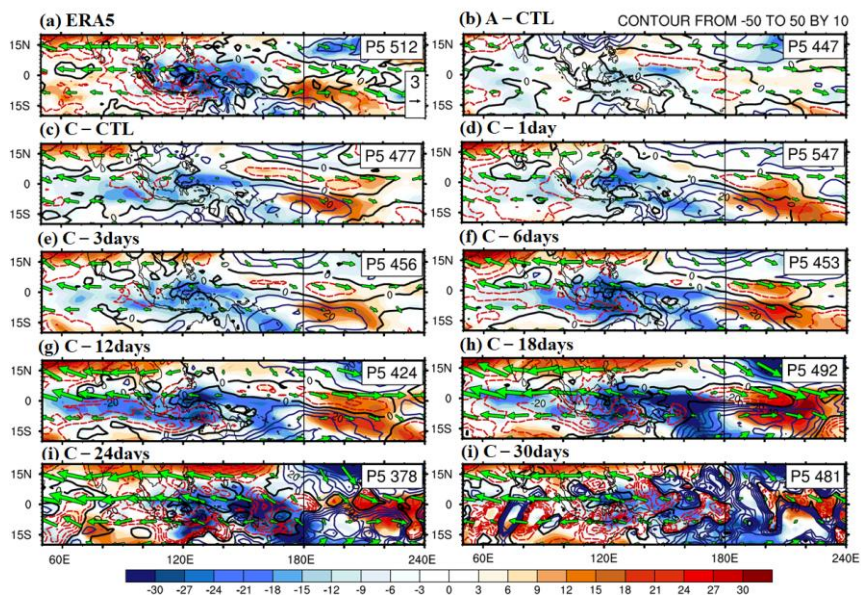


1175

1176 **Figure 11.** The projection of each MSE component onto the ERA5 column-integrated
 1177 MSE tendency at phase 5 over the MC (20° S–20° N, 90–210° E): $\langle dmdt \rangle$, $-$
 1178 $\langle wmdp \rangle$, $-\langle vdm \rangle$, Qr, Fs, and residual; decomposition of horizontal MSE advection
 1179 to zonal and meridional advection ($-\langle udmdx \rangle$ and $-\langle vdmdy \rangle$).

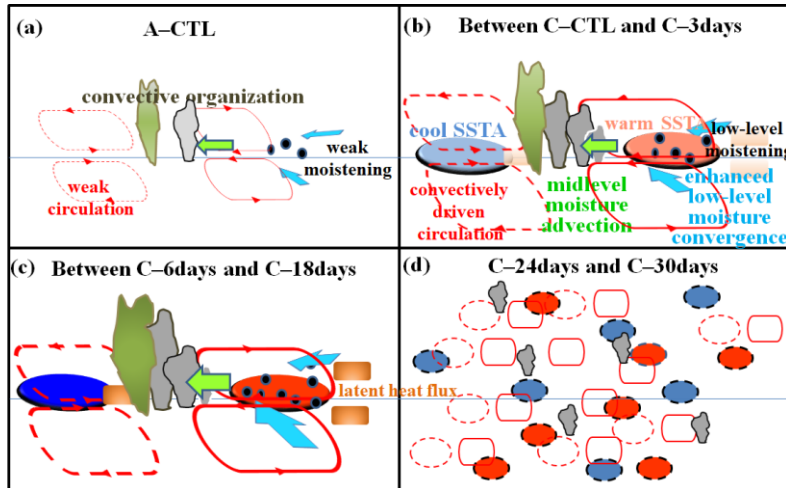


已删除:



1181

1182 **Figure 12.** Filtered column-integrated vertical ($\text{J kg}^{-1} \text{s}^{-1}$, shading) and horizontal
 1183 MSE advection ($\text{J kg}^{-1} \text{s}^{-1}$, contours interval 6.0), and 200-hPa wind (green vector
 1184 with reference vector 3 m s^{-1}): (a) ERA5, (b) A-CTL, (c) C-CTL, (d) C-1day, (e)
 1185 C-3days, (f) C-6days, (g) C-12days, (h) C-18days, (i) C-24days, and (j) C-30days.
 1186 Solid-blue, dashed-red, and thick-black curves represent positive, negative, and zero
 1187 values, respectively.



1189

1190 **Figure 13.** Schematic diagrams illustrate the anomalous circulation and moistening
 1191 processes during the eastward propagation of the MJO in experiments: (a) A-CTL, (b)
 1192 high-frequency SST feedback experiments (C-CTL, C-1day, and C-3days), (c) low-
 1193 frequency SST feedback experiments (C-6days, C-12days, and C-18days), and (d)
 1194 C-24days and C-30days experiment. In each panel, the horizontal line represents the
 1195 equator. The size of clustering gray clouds indicates the strength of convective
 1196 organization. A red ellipse indicates convection-driven circulation. In the coupled
 1197 simulations, light red (blue) filled ovals represent warm (cold) SST anomalies,
 1198 respectively, and grass green filled rectangle represent latent heat flux. Unresolved
 1199 convective processes are indicated by black dots representing low-level moisture
 1200 convergence. Low-level moisture convergence into the equatorial trough is shown by
 1201 light blue arrows, while midlevel moisture advection is represented by left-pointing
 1202 green arrows. The deeper colors or thicker lines on the map indicate stronger anomalies
 1203 of the MJO perturbations. Note: The concept of the figure is based on DeMott et al.
 1204 (2014).